Gene expression patterns of the developing human face at single cell resolution reveal cell type contributions to normal facial variation and disease risk

Nagham Khouri-Farah[1], Emma Wentworth Winchester[1], Brian M. Schilder[2,3], Kelsey Robinson[4], Sarah W. Curtis[4], Nathan G. Skene[2,3], Elizabeth J. Leslie-Clarkson[4], Justin Cotney[5,6]

Affiliations

1 Graduate Program in Genetics and Developmental Biology, UConn Health

2 Department of Brain Sciences, Faculty of Medicine, Imperial College London, London, W12 0BZ, UK

3 UK Dementia Research Institute at Imperial College London, London, W12 0BZ, UK

4 Department of Human Genetics, Emory University School of Medicine, Atlanta, GA 30322, USA

5 Department of Surgery, Children's Hospital of Philadelphia, Philadelphia, PA

6 Perelman School of Medicine, University of Pennsylvania, Philadelphia, PA

Abstract

Craniofacial development gives rise to the complex structures of the face and involves the interplay of diverse cell types. Despite its importance, our understanding of human-specific craniofacial developmental mechanisms and their genetic underpinnings remains limited. Here, we present a comprehensive single-nucleus RNA sequencing (snRNA-seq) atlas of human craniofacial development from craniofacial tissues of 24 embryos that span six key time points during the embryonic period (4–8 post-conception weeks). This resource resolves the transcriptional dynamics of seven major cell types and uncovers distinct major cell types, including muscle progenitors and cranial neural crest cells (CNCCs), as well as dozens of subtypes of ectoderm and mesenchyme. Comparative analyses reveal substantial conservation of major cell types, alongside human biased differences in gene expression programs. CNCCs, which play a crucial role in craniofacial morphogenesis, exhibit the lowest marker gene conservation, underscoring their evolutionary plasticity. Spatial transcriptomics further localizes cell populations, providing a detailed view of their developmental roles and anatomical context. We also link these developmental processes to genetic variation, identifying cell type-specific enrichments for common variants associated with facial morphology and rare variants linked to orofacial clefts. Intriguingly, Neanderthal-introgressed sequences are enriched near genes with biased expression in cartilage and specialized ectodermal subtypes, suggesting their contribution to modern human craniofacial features. This atlas offers unprecedented insights into the cellular and genetic mechanisms shaping the human face, highlighting conserved and distinctly human aspects of craniofacial biology. Our findings illuminate the developmental origins of craniofacial disorders, the genetic basis of facial variation, and the evolutionary legacy of ancient hominins. This work provides a foundational resource for exploring craniofacial biology, with implications for developmental genetics, evolutionary biology, and clinical research into congenital anomalies.

Main

Craniofacial development orchestrates the formation of the human face through the interplay of multiple cell lineages. These cell types, including mesenchyme, ectoderm, endothelium, and cranial neural crest cells (CNCCs), differentiate into a diverse array of tissues such as bone, cartilage, muscle, skin, and vasculature[1-3]. Together, these cells and tissues give rise to the face's essential functions like respiration, mastication, communication, and sensory perception[4-7], Disruptions to craniofacial developmental processes rank amongst the most common causes of human congenital anomalies, with orofacial clefts representing a significant portion of global birth defects[8-11]. Thus, there exists significant need to understand the molecular, genetic, and cellular mechanisms underlying craniofacial development in humans.

Studies utilizing model organisms, particularly mice, have offered key insights into craniofacial development and abnormalities[12-16]. However, significant differences exist between mouse and human craniofacial development, including variations in timing, cellular contributions, and gene regulatory networks[1,13,17-22]. Furthermore, human craniofacial features exhibit evolutionary adaptations that distinguish them from other mammals and primates, underscoring the necessity for human-specific studies [5,13,21,22].

Advances in single-cell and single-nucleus RNA sequencing (scRNA-seq and snRNA-seq respectively) technologies have enabled detailed characterization of cellular diversity and gene expression during development[12,15,23-27]. These tools are particularly valuable for resolving the dynamics of rare or transient cell populations, such as CNCCs, that play critical roles in craniofacial formation[13]. While previous efforts have developed single-cell atlases for murine craniofacial tissues, corresponding human datasets have been limited by sample availability, insufficient temporal resolution, and challenges in profiling craniofacial-specific populations[12,15,23]. Only a few studies have examined bulk gene expression patterns and regulation specifically during human craniofacial development[13,14,28-31], and only two datasets are currently available during the embryonic period of human development[13]. While mapping of human genetics findings to mouse craniofacial cell types has indicated potential disease-causing subtypes[32], the limited number of replicates underlying the mouse data and differences between human and mouse craniofacial development preclude confident interpretation.

To address these gaps in knowledge, we constructed a time-resolved gene expression atlas of human craniofacial development when the bulk of human craniofacial development occurs[33,34]. Using snRNA-seq on craniofacial tissues from 24 individual human embryos encompassing six key time points from 4 to 8 post-conception weeks, we profiled over 42,000 nuclei and identified seven major cell types, including mesenchyme, ectoderm, endothelium, muscle progenitors, and CNCCs. Integration with human spatial transcriptomics further validated the localization of these subtypes within the developing human face. Comparative analysis with murine craniofacial datasets generated here and previously published[23] highlighted significant conservation of major cell types and their gene expression programs, alongside species biased markers that reflect differences in mouse and human biology.

Beyond the developmental biology of craniofacial formation, this study explores the genetic and evolutionary factors shaping human craniofacial features. By integrating genome-wide association studies (GWAS) with our atlas, we identified cell type-specific enrichments for genetic variants

associated with normal facial variation. We found that specific subtypes of ectoderm and mesenchyme, likely spatially restricted, contribute to different aspects of facial appearance and shape. We also examined rare variants associated with congenital craniofacial disorders such as orofacial clefts. We find that *de novo* protein damaging variants identified in orofacial clefting trios are enriched in genes that specify distinct cell subtypes in the face. This enrichment was heavily biased toward ectodermal subtypes that is largely obscured in previous analyses based on bulk chromatin and gene expression[13,35-38]. We find the damaging variants coalesce in the ectodermal derived nasal placode implicating this early structure in orofacial clefts. Our analysis also uncovered evidence linking Neanderthal-introgressed sequences to genes with biased expression in specific craniofacial cell types.

This comprehensive atlas provides a high-resolution view of the cellular and molecular landscape of human craniofacial development, integrating gene expression, spatial mapping, and evolutionary genomics. Our work not only enhances our understanding of human craniofacial biology but also establishes a framework for future studies aimed at uncovering therapeutic targets and evolutionary insights into one of the most defining features of human anatomy. This data can be explored through an interactive web application that is accessible to most researchers: https://cotneyshiny.research.chop.edu/shiny-apps/craniofacial_all_snRNA/ as well as alongside the growing number of single cell datasets hosted at the Chan-Zuckerberg CellXGene Discover resource[39].

Results

Time-resolved atlas of gene-expression in the developing human face

To characterize the cellular landscape of human craniofacial development we performed snRNA-seq analysis of 24 individual human embryos across 6 distinct time points, encompassing major milestones of human craniofacial development from 4 to 8 post conception weeks (Fig. 1A). We profiled the entire craniofacial prominence from multiple biological replicates at each time point resulting in 86,359 individual nuclei after filtering for doubles and quality of per nucleus data. While experiments in mouse offer precise control of tissue sampling for downstream processing, samples obtained from human embryos are more difficult to control what is collected. To identify potential biases or nuclei obtained from extraneous tissues we performed initial clustering of all samples to identify potential extraneous cell types. This analysis revealed a total of 13 distinct clusters (Fig. S1a). This number of clusters was substantially higher than the main cell types identified in mouse craniofacial developmental studies, suggesting that the human samples potentially contained extraneous tissues that are not part of the craniofacial complex[12-14]. When we examined the contributions of individual samples to these clusters, we found several clusters that were made up of nuclei derived from a small number of samples (Fig. S1b). Closer inspection of the genes strongly expressed in these clusters revealed many canonical neuronal genes, such as *TUBB3* and *MAP2* (Fig. S1c-d). We reasoned these clusters were derived from developing brain tissue not directly part of the craniofacial structures. We therefore excluded these nuclei from downstream analyses resulting in a total of 42,131 remaining nuclei with an average of 4095 nuclei from each sample (Fig. S2a) and a median of 7500 counts from 2250 genes per nucleus (Fig. S2b and c). We observed that early samples had consistently higher mitochondrial reads (Fig. S2d), potentially reflecting their higher dependence on mitochondrial output or an artifact related to lower cell numbers in the processing of each sample.

To determine the quality of these filtered samples we sought to compare to other well characterized gene-expression profiles of craniofacial development. Our previous studies of bulk gene expression during human craniofacial development revealed a strong time related component across the samples[13]. When we combined gene expression profiles from all nuclei of a specific stage into pseudo-bulk gene expression profiles individual replicates were well correlated with others at the same time-point and less so with samples with greatest differences developmental time across this time course (Fig. S3). Principal component analysis of these pseudo-bulk profiles largely recapitulated our previous results with the first principal component ordering samples readily by known stage of development (Fig. 1B, Fig. S4a). Furthermore, when we performed differential expression between the pseudobulk samples we found very similar results to those obtained by bulk gene expression between the same timepoint comparisons (Fig. S4b). Specifically, the greatest number of differentially expressed genes were observed between the earliest and latest timepoints that could be compared across the two data sets (CS13 vs CS17) (Fig. S4c). Overall, these results suggest that our single-nucleus expression data closely resembles the bulk gene expression data that we have previously shown is enriched for many aspects of craniofacial biology and developmental abnormalities relative to many other tissues and cell types[13].

Identification of major cell types present in craniofacial development

Having established that the single nuclei profiles at the pseudobulk level captured many of the expected aspects of craniofacial biology, we proceeded to re-cluster the filtered nuclei to first identify the major cell types present in the developing face. We identified seven major clusters and projected these high-dimensional data into two dimensions using Uniform Manifold Approximation and Projection (UMAP)[40] (Fig. 1C). The clusters were contributed to by samples from each of the replicates and stages in very similar proportions (Fig. 1D and E). Interestingly, this was two more distinct clusters than previously characterized in the E11.5 mouse craniofacial structures[12]. We reasoned that this could be due to differences in human and mouse development, but most likely related to the additional replicates and timepoints and how tissues were collected and processed. To address this, we first examined expression of the five genes examined by Li et al, *ALX1*, *EPCAM*, *HEMGN*, *CDH5*, and *FCERG1* as markers of mesenchyme, ectoderm, blood, endothelium, and immune cells respectively (Fig. 2A). *ALX1* was most strongly expressed in cluster 1, *EPCAM* in cluster 2, *HEGMN* in cluster 4, *CDH5* in cluster 5, and *FCERG1* in cluster 7, while clusters 3 and 6 did not show signal for any of these genes. While some of the timepoints were derived exclusively from female and male samples, CS12 and CS13 respectively, we did not observe any significant bias is these main cluster (Figure S2E).

In an attempt to characterize these unknown clusters we first identified the top 10 genes that were most strongly differentially expressed between the individual clusters (Fig. 2B, Supplemental Table 1). Cluster 1 was marked by *PDGFRA, TWIST1, and PRRX1,* consistent with identifying this cluster as mesenchyme[41,42]. Cluster 2 was identified by *GRHL2* and *ESRP1*, genes that have been reported to be specifically active in surface ectoderm and epithelial cells[43-46]. Cluster 4 was marked by *SPTA1, ALAS2, RHAG,* genes involved in erythrocyte function[47-51]. Cluster 5 showed highly biased expression for *KDR and FLT1,* genes associated with the vascular system and endothelium function[52,53]. Cluster 7 was marked by *PTPRC*, *CD86,* and *CD136,* consistent with immune cell function[54-56]. These all confirmed the initial identities suggested by the markers described by Li et al in E11.5 mouse craniofacial tissue. The

unknown cluster 3 showed highly biased expression of *MYOG*, *MYL1*, and *MYH3*, all genes related to muscle specification and function[57-59]. The unknown cluster 6 showed strongly biased expression for *CDH19*, *INSC*, and *MMP17*. These genes are involved in a variety of biological processes including cell adhesion, spindle orientation during mitosis, and degradation of extracellular matrix[60-62]. We also noted specific expression of *FOXD3,* a developmental transcription factor which has been linked to pluripotency maintenance in stem cells and specification of neural crest in multiple species[63-66].

We then analyzed the top 100 marker genes from each cluster for gene ontology, pathway, and disease enrichments. The genes that identified putative mesenchyme cluster 1 were enriched for a number of biological process categories related to skeletal, cartilage, and roof of mouth development (Fig. S5A, Supplemental Table 2); cellular components related to collagen processing (Fig. S5B, Supplemental Table 3); molecular functions related to gene expression, extracellular matrix, and collagen binding (Fig. S5C, Supplemental Table 4); pathways related to production of extracellular matrix (Fig. S5D, Supplemental Table 5); and diseases including cleft palate and frontonasal dysplasia (Fig. 2C, Supplemental Table 6).

Genes most strongly expressed in cluster 2, likely ectoderm, were enriched for biological process categories related to tight junction assembly and cell adhesion (Fig. S5A, Supplemental Table 2); cellular components related to the plasma membrane (Fig. S5B, Supplemental Table 3); molecular functions related to cadherin and laminin binding (Fig. S5C, Supplemental Table 4); pathways related to tight junction and Hippo signaling (Fig. S5D, Supplemental Table 5); and diseases including epithelioma and keratoderma (Fig. 2C, Supplemental Table 6).

Putative muscle progenitor cluster 3 marker genes were enriched for biological processes related to muscle cell differentiation (Fig. S5A, Supplemental Table 2); cellular components of the sarcomere (Fig. S5B, Supplemental Table 3); molecular functions related to actin filament binding (Fig. S5C, Supplemental Table 4); calcium signaling pathways (Fig. S5D, Supplemental Table 5); and diseases including myopathic abnormalities and muscular dystrophy (Fig. 2C, Supplemental Table 6).

The markers of red blood cell cluster 4 were enriched for biological processes related to erythrocyte homeostasis and oxygen transport (Fig. S5A, Supplemental Table 2); cellular components of the hemoglobin complex (Fig. S5B, Supplemental Table 3); molecular functions related to heme and oxygen binding (Fig. S5C, Supplemental Table 4); pathways involved in Malaria response and mineral absorption (Fig. S5D, Supplemental Table 5); and diseases including hemolytic anemia and beta thalassemia (Fig. 2C, Supplemental Table 6).

Genes with highest expression in putative endothelium cluster 5 were enriched for biological processes related to endothelial cell differentiation and proliferation (Fig. S5A, Supplemental Table 2); cellular components including plasma membrane rafts and caveola (Fig. S5B, Supplemental Table 3); molecular functions related to Notch and guanyl nucleotide binding (Fig. S5C; Supplemental Table 4); pathways involved in fluid shear stress and atherosclerosis (Fig. S5D; Supplemental Table 5); and diseases of the capillaries and hemangiomas (Fig. 2C, Supplemental Table 6).

Immune related cluster 7 marker genes were enriched for biological processes related to cytokine production and immune response (Fig. S5A, Supplemental Table 2); cellular components including

specific and tertiary granule membranes (Fig. S5B, Supplemental Table 3); molecular functions related to Toll−like receptor binding and immunoglobulin receptor activity (Fig. S5C, Supplemental Table 4); pathways related to the phagosome and complement and coagulation cascades (Fig. S5D, Supplemental Table 5); and diseases including many types of infections and immunodeficiencies (Fig. 2C, Supplemental Table 6).

We then turned to the not yet concretely identified cluster 6. The marker genes we identified for this cluster were enriched for biological processes related to glial cell differentiation and myelination (Fig. S5A, Supplemental Table 2); cellular components including plasma membrane signaling receptor complexes and exocytic vesicles (Fig. S5B, Supplemental Table 3); molecular functions related to protein tyrosine kinase activator activity (Fig. S5C, Supplemental Table 4); and diseases related to central nervous system disorders and neuropathies (Fig. 2C, Supplemental Table 6). We did not detect any significant pathway enrichments for this particular cluster.

Identification of presumptive human cranial neural crest

The marker gene ontology analysis successfully confirmed the identity of six of the seven major clusters. However, cluster 6 remained difficult to identify due to the variety of enrichments identified amongst marker genes. Beyond the more nervous system-oriented enrichments listed above we also found significant biological and disease enrichments that were shared with the mesenchyme and muscle clusters. This included enrichments for extracellular matrix organization and binding, cell adhesion via plasma-membrane, skeletal muscle system development, and several types of tumors (Fig. 2C, Fig. S5A-D, Supplemental Tables 2-6). When we more closely inspected biological process categories identified for cluster 6, we observed additional enrichments related to Schwann cell development and melanocyte differentiation (Supplemental Table 2). Closer inspection of full disease enrichments for this cluster revealed several types of Waardenburg Syndrome, Hirschsprung Disease, and demyelination disorders (Supplemental Table 6). The wide variety of biological functions and specific disease enrichments all suggested that this cluster might be enriched for neural crest cells. Marker genes driving these enrichments included *EDNRB*, *ERBB3*, *PAX3*, *SOX10*, *SPP1*, *TFAP2B*, and *ZEB2*, genes well known to be involved in various aspects of neural crest specification and migration[67]. However, while these genes are biased toward cluster 6 relative to other clusters, they are not exclusively expressed in cells found in this cluster (Fig. S6A). Amongst these *ZEB2* is more broadly expressed across all clusters except for ectoderm. Further inspection of marker genes revealed that while some of these genes are indeed strongly biased toward cluster 6, only a small percentage of cells from this cluster express each gene (Fig. S6B). Qualitatively, expression of each of these genes could be observed outside of cluster 6 and potentially in subclusters of the main clusters we have defined thus far (Fig. S6C). Given the heterogeneity of expression of each of these marker genes we reasoned that jointly analyzing expression of a module of genes might be a better indicator of cell type identity as has been shown in other single cell-based studies[68]. When we examined a module of genes from regulatory networks recently identified in cultured human and chimpanzee cranial neural crest cells (CNCCs) [69], we found significantly higher expression in cluster 6 (Fig. 2D). Together these results strongly point to this cluster being enriched for putative CNCCs.

Thus far few studies have been able to identify significant populations of CNCCs from primary human tissue[70-72]. To better understand the gene expression programs that are active in these cells we first performed subclustering on these cells (n = 1821). We identified 11 distinct subclusters from this original population (Fig. 3A). The seven main clusters derived from the largest numbers of cells were annotated as CNCCs, while the four more punctate clusters were initially annotated as CNCC like (cnl). These clusters consisted differentially of cells derived from each of the stages profiled. Those clusters that were heavily biased toward CS12 were labeled as early (eCNCC), those that were biased toward CS13-C16 as intermediate (iCNCC), and those that were derived primarily from the CS17 and CS20 timepoints as late (lCNCC) (Fig. 3B). When we examined gene expression of many CNCC markers from the literature we found variable patterns of expression. *SOX10* expression was observed in all of the CNCC and cnl clusters along with *NR2F1* and *NR2F2,* two genes identified as master regulators of CNCC fate[6,73] (Fig 3C). *TFAP2A* was expression was observed in all clusters but was considerably lower in the late CNCCs. Its ortholog *TFAP2B* was conspicuously absent from one late CNCC cluster (lCNCC2) and from cluster cnl2 (Fig. 3C). *ETS1* and *FOXD3* were generally expressed in most subtypes, but both expressed at very low levels in lCNCC1 (Fig. 3C). PAX3 expression was more variable but in populations distinct from the two previously mentioned transcription factors. *SOX9* and *COL20A1* were more specifically expressed across the clusters, but again in non-overlapping patterns.

Overall, these genes largely confirmed that the cells we identified have neural crest character, however they did not display distinct patterns across the clusters precluding easy identification of these putative subtypes. To identify genes that readily identified each of these subtypes, we repeated the marker gene identification performed on the main types above. We identified approximately 2000 genes that were differentially expressed across these subclusters with an adjusted p-value cutoff less than 0.05 and a $\log_2$ fold change greater than one (Supplemental Table 7). The top five marker genes in each subtype revealed multiple transcription factors that distinguish each cluster. These included *SOX21* in early CNCCs, *MKX* in intermediate CNCCs, *HAND2* in late CNCCs, and *NKX2-1*, *ALX4*, and *FOXL1*, in clusters cnl1, cln2, and cnl3, respectively (Fig. 3D). Identification of enriched gene ontology categories for each subtype revealed distinct functions for each. Marker genes of early CNCCs were enriched for process related to early pattern specification and axon guidance. Intermediate CNCC clusters were enriched for functions related to extracellular matrix organization and skeletal system development. Late CNCC clusters were enriched for various channel activity and sympathetic nervous system development. The cnl1 cluster was enriched for several categories shared with eCNCC1 suggesting this was an early multipotent neural crest type. The cnl4 cluster was very specifically enriched for functions related to pigment granules and melanin biosynthesis indicating these were melanocytes, a cell-type derived from neural crest (Figure S7, Supplemental Tables 8-11).

Thus far our analysis has lacked spatial localization, making it unclear where these cell types are derived or reside in the intact human embryo. Recently published spatial transcriptomics on two sections of a human CS13 provided an opportunity to identify such patterns of expression[25]. We reprocessed this data, merged all the cells from both sections, identified cell types, and confirmed their spatial locations (Figure S8). We then examined expression of marker genes that identified CNCCs versus the other major craniofacial cell types. *NR2F1* was broadly expressed across the embryo whereas *PAX3*, *TFAP2A*, and *TFAP2B* were more regionally restricted to the head and neural tube regions (Fig. 3E).

Genes identified as markers of CNCC subtypes showed a variety of patterns of expression. *ALX4* was generally restricted to the head region and putative frontal nasal process region. *CRABP1* was found in the anterior neural tube, eye region, and the limb. *HAND2* expression was observed in putative pharyngeal arch regions, heart, and limb. *NKX2-1* had highly restricted expression in a location that could represent a fusion zone between the lateral nasal prominence and the maxillary prominence (Fig. 3E). We then calculated module scores on these spatial data using the marker genes from each of the CNCC subtypes. We found that at this stage of development, each of these sets of marker genes were generally biased toward the neural tube region of the embryo with cnl1 marker genes showing the most restricted pattern of expression.

Conservation of cell types and gene expression programs in human and mouse craniofacial development

The analysis above showed compelling evidence of the identities of the major cell types in the developing human face. This included two cell types, muscle and CNCCs, not previously observed in single cell atlases of mouse craniofacial development[12,15,23]. We wondered whether these cell types were not present in these mouse datasets due to sampling differences in tissues and broader timepoints. To address this, we generated single-nucleus gene expression data from mouse craniofacial tissues harvested from multiple biological replicates of E10.5 to E12.5. These samples reflected the major morphological landmarks of the human tissue profiled allowing a more direct comparison of cell types. We then further combined this data with recently published single cell gene expression data from E13.5 and E15.5 resulting in 79402 expression profiles after similar quality control filters applied to human data (Methods). When we clustered these data using approaches identical to the human data, we obtained the same number of main clusters with remarkably similar cluster ratios and organization in the UMAP projection space (Fig. 4A, Supplemental Table 12). When we examined gene expression of the same major markers profiled in human (Fig. 2A) we readily identified the same major mouse cell types including muscle and putative CNCCs (Fig. 4B). Roughly 70% of the tissue was of mesenchymal origin, 15% was ectodermal, and the remaining 15% was distributed similarly across the remaining 5 cell types. When we projected these cell types on our recent analysis of spatial gene expression in mouse E15.5 craniofacial sections, we found expected patterns of cell type localization (Fig. 4C). To determine if these cell types were specified by the same sets of genes, we compared marker gene identities obtained in the same fashion in both species. We found significant sharing of marker genes between the orthologous major cell types (Fig. 4D). The highest degree of sharing was found between mesenchyme, followed by endothelium and ectoderm. While still significant, the lowest degree of marker gene conservation was observed between CNCCs of each species (Fig. 4D). When we examined the functionally conserved marker genes for ontology enrichments, we observed distinct patterns of enrichment that confirmed the cell type assignments in each species (Fig. S9A-E, Supplemental tables 13-17). Disease enrichments related to general craniofacial abnormalities were observed in mesenchyme, while enrichment of cleft upper lip was observed in conserved markers of mesenchyme and ectoderm (Fig. S9F, Supplemental Table 18). These enrichments were driven by well-known craniofacial genes including *ALX1*, *ALX4*, *MSX1*, *RUNX2*, and *TWIST1* reinforcing their conserved role in mammalian craniofacial development (Supplemental Table 18).

Species-specific differences in marker gene expression during human and mouse craniofacial development

While the overall craniofacial cell types and major gene expression patterns were shared between species, our analysis revealed hundreds of marker genes that were only called in a single species (Supplemental Tables 19-21). The largest fraction of species biased calls was observed for CNCCs. As expected, the shared CNCC markers were enriched for functions related to gliogenesis and nervous system development. However, the human-biased markers were biased toward genes related to ribosome biogenesis and cytoplasmic translation while mouse-biased markers were enriched for genes with functions related to oxidative phosphorylation and the electron transport chain (Figure S10A-D). When we examined the mesenchyme cluster, we found the shared markers were enriched for morphogenesis and differentiation programs for mesenchymal derived cell tissues as expected. However, human-biased markers were enriched generally for functions related to DNA replication and cell cycle while mouse-biased markers were enriched for only a few categories primarily related to MAPK signaling pathways (Figure S11 A-E). When we examined the human disease phenotypes enriched for each of these gene sets, we found general craniofacial abnormalities and isolated cleft palate among conserved genes. Mouse-biased mesenchymal markers were enriched exclusively for multiple seizure disorders. Human-biased mesenchymal markers were enriched for a number of craniofacial related phenotypes including microphthalmos and low set ears and exclusively for sloping forehead, large nose, and biparietal narrowing (Figure S11D). Given these phenotypes, genes driving these enrichments could be significant contributors to differences in skull shape, size, and function between human and mice. When we inspected these categories, we found genes with the highest levels of specificity for human mesenchyme included *ALX3*, *CTSK*, *CYP1B1*, *FOXC1*, *MAB21L1*, *MSX2*, and *TENM1* (Fig. 4E).

Leveraging mouse craniofacial cell-type annotations to identify human craniofacial subtypes.

Having demonstrated that major cell types, including the CNCCs, could be readily identified in both species and showed significant conservation of gene expression, we reasoned we could leverage the substantial annotation resources that have been generated for mouse to identify human cell subtypes. To achieve this, we focused on the major cell types that have been extensively subclustered and characterized in previous publications[12,23,74], mesenchyme and ectoderm, as well as the novel populations of CNCCs we have identified here. When we performed subclustering of mouse CNCCs, we identified 8 distinct subtypes (Fig. 4F). These had a very similar arrangement in UMAP space compared to the subclusters we identified in the human CNCCs (Fig. 3A). When we examined functional enrichment of marker genes of each of these subclusters we found similar results as in human, including a clear population of melanocytes (Fig. 4G, Supplemental Table 22). Examination of the same neural crest markers as in human CNCC subtypes revealed very similar patterns of expression (Fig. 4H). We observed that *Sox10* and *Nr2f2* were expressed across all the subtypes as well as a similar trend in variable expression of *Foxd3*, *Pax3*, *Tfap2a*, and *Tfap2b* and across subtypes. When we inspected the markers for each of these subtypes, we found many of the same genes as in human subtypes including *Alk*, *Alx4*, *Crabp1*, and *Hand2* (Fig. 4I, Supplemental Table 23). When we reprocessed mouse E11.5 spatial transcriptomic data[43] in a similar fashion to the human CS13 data, we found very similar patterns of expression for many of the human CNCC markers in mouse tissues (Figure S12A). Examination of module scores calculated from the mouse CNCC subtypes also revealed similar patterns across the

mouse embryo as observed for human (Figure S12B). To attempt to identify the orthologous CNCC subtypes across species we compared sharing of orthologous marker genes much as we did with the main cell types. When we examined a confusion matrix of comparisons of cell types we found the highest similarity amongst CNCC subclusters human iCNCC4 and mouse iCNCC2 as well as human cnl4 and mouse cnl, the putative melanocyte clusters (Fig. S13A). The additional cnl clusters in human showed variable similarity to mouse and could reflect heterochrony, primate cell states not present in rodents, or the more genetically diverse human samples profiled.

Having demonstrated that even in the potentially least conserved cell type that we could readily identify shared subtypes across species we then turned to the other major cell types, mesenchyme and ectoderm. We subclustered the large mouse mesenchyme cluster and identified 19 subclusters across the mouse timeseries. Using a combination of gene ontology enrichments of marker genes and previous annotations of mouse craniofacial single cell and spatial transcriptomics we assigned functional and/or positional labels to each cluster (Fig. 4J, Supplemental Tables 22 and 24-27). For example, the well-established lateral nasal process (LNP) marker *Pax7*[12,75-77] and the osteoblast marker Sp7[78,79] were used to define respective clusters. In the case of osteoblasts we observed two clusters expressing similar markers but were biased in cells from different stages of development, thus we further refined these as early and late osteoblasts (Figure 4K). Two small clusters clearly represented contaminating blood derived cells or neuronal-like populations while one additional cluster could not be readily identified but had many markers associated with rapidly cycling cells (Fig. 4K). When we examined the mouse E11.5 spatial transcriptomics data we had reprocessed above, we found good concordance between marker gene expression and generalized localization in the embryo (Figure S14A). In contrast to both the human and mouse CNCC analysis, projection of modules scores for mouse mesenchymal clusters readily identified specific regions of the developing craniofacial structures that corresponded well to labels we had assigned them (Fig. 4L and S14B).

We performed identical analyses for the ectodermal cluster revealing an additional 19 subclusters (Fig. 4M). Applying the same analysis of marker genes from the literature, gene ontology enrichments, and expression in mouse single cell transcriptomics data we annotated each of these clusters with functional and spatial labels (Supplementals Tables 22 and 24-27). We identified highly specific ectodermal populations like periderm marked by *Gabrp*[12,80,81] , cells that will form structures of the inner ear marked by Oc90 (Zhao et al 2007, Wang PNAS 1998), palate ectoderm identified by *Foxe1*[82], and the putative pituitary marked with *Lhx3* and *Lhx4*[83,84] among others (Fig 4N). As with the mesenchyme, we found the spatially resolved expression of marker genes corresponded well to expected positions of the mouse embryo (Figure S15A). Module score calculations for each subtype resulted in refined spatial identification of subtypes that matched the labels and expected positions well (Fig. 4O and S15B).

While the module score analysis is indicative of the cell types and spatial locations of the labels we applied, they are calculated independently of any other cell types. We therefore sought to predict what are the dominant cell types in specific locations based on spatial transcriptomics data we had not used for any of the previous analysis. When we projected top spatial predictions for 20 of the subtypes identified across previously published E15.5 mouse head data[23,85] we found very good concordance for cell type labels and known anatomical features (Figure 4P). Overall, the analyses performed here

confirmed the identities of multiple cell types across the development of mouse craniofacial tissues. Moreover, the demonstration of conserved marker genes provides a framework for transferring cell type labels to subclusters identified in human data as well as putative spatial inferences from data that originally lacked that information. We explore the subtype identifications in human data below.

Characterization of mesenchymal cell subtypes

When we subclustered the large number of mesenchymal cells, we identified 22 subtype clusters. Using the same confusion matrix-based approach from above based on orthologous gene expression in mesenchymal subtypes, we assigned cell type and/or functional labels to each of the human clusters (Fig 5A and S13B). In some cases, multiple human clusters correlated well with a single mouse cluster and were labelled as separate populations (e.g., mouse mandibular arch and human mandibular arch 1-3). The most abundant cell types were obtained from the mandibular arch and the maxillary process and were well represented from each of the timepoints. Some of the transient structures like the lateral nasal process and cells labeled as early osteoblasts were biased towards early timepoints, while later forming cell types and structures such as cartilage and palatal shelves were dominated by cells derived from CS20 samples (Fig. 5B). When we examined marker genes identifying each of these clusters we found many transcription factors including *BARX1*, *MSX1*, and *MSX2* in the maxillary process population 2 cluster (MxP2); *SHOX* in mandibular arch 1 (arch1); *PAX7* in lateral nasal process population 2 (LNP2); *SPX* in palatal fusion zone population 1 (palatal.fusion.1); *HAND1* in mandibular arch population 3 (arch3); *HOXA3*,*B3*, and *D3* in fusion mesenchyme population 1 (fusion.mes.1); *MKX* in palatal shelf population 1.1 (palatal.shelf.1.1); and *TBXT* in cartilage population 2 (cartilage.2) among many others (Fig. 5C).

Gene ontology analysis revealed many biological processes, cellular component, and molecular process categories that were relevant for these subtypes (Figure S16). For example, cartilage1 and cartilage2 were differentially enriched for hyaluronic acid and frizzled binding respectively. Cartilage 1 is primarily found in CS20 samples suggesting these are distinct stages of cartilage development. Early osteoblast markers were enriched in pathways regulating pluripotency while late osteoblast markers were enriched for PI3K-AKT signaling and parathyroid hormone response. The more regional based annotations shared many of the same functional enrichments suggesting the same underlying processes were active in these cell types. However, the maxillary process / anterior lateral nasal process derived cells (MxP.aLNP) likely from near the lambdoid junction[86]showed substantially higher expression of many genes related to ribosome production and cytoplasmic translation. Examination of disease enrichments across cluster marker genes revealed some tissue-specific disorders like Osteogenesis imperfecta in late osteoblasts and epiphyseal dysplasia in cartilage 1. Enrichment for genes related to isolated cleft palate were found in several clusters including MxP2, palatal.shelf2.1, palatal.shelf.2.2, and cartilage 1 (Fig 5D).

While the gene ontology analysis confirmed the labeling of some specific cell types, the more positional types remained less clear. To address this, we again turned to the CS13 human spatial transcriptomics data. When we examined some of the markers that defined the mesenchyme versus other cell types, such as *TWIST1* and *PRRX1*, we found fairly broad expression across the embryo with some bias toward the craniofacial region. Other markers like *SATB2* were much more regionally restricted and potentially specifically mark craniofacial mesenchyme versus other types (Fig. 5E). When we examined some of the

subtype marker genes, we found much more regionalized expression. *MSX1* was found near many surface locations with a bias toward the head. *BARX1* was rather specifically localized in the general region of the pharyngeal arches and the developing stomach. *SPX* and *CYP26C1* were both restricted to the head region of the embryo at this stage (Fig. 5F). As was observed in mouse, we found much more regionalized signals from module scores for each subtype. The mandibular arch clusters were clearly enriched in the pharyngeal arch region of the CS13 embryo and biased toward the more anterior portion of this region. The lateral nasal process clusters were enriched in distinct areas of the head with LNP1 being more posterior and LNP1 being more anterior. Other subtypes like MxP2 and palatal.shelf2.2 showed good spatial concordance with the labels that had been assigned (Fig. 5G).

Characterization of ectodermal cell subtypes

We then turned to the ectodermal cluster to identify potential subtypes. Using the same basic approach as the mesenchyme, we identified 22 distinct ectodermal clusters (Fig. 6A). Transferring of mouse labels (Figure S13C) revealed cells that would give rise to specific ectodermal-derived organs like the pituitary and thyroid, structures of the inner ear (auditory1-3), and surfaces of several structures including periderm (Fig. 6A). As with mesenchymal subclusters, many of the ectodermal subclusters annotated as early versus late had biased sample contributions (Fig. 6B). Amongst marker genes of ectodermal subtypes, transcription factors were again prominent. *LHX3*, *SIX6*, and *PITX2* were most strongly expressed in the pituitary; *GATA6* marked the palate subtype; the nasal placode (NaP) was identified by *SP8* and *FEZF1*; auditory subtypes 1-3 were marked by *SALL3*, *GRIN2A*, and *SP9* respectively; *EBF1*, *EBF2*, and *EBF3* in a single ectodermal subtype (ect.EBF); and *TBX18* marked a putative fusion zone cluster among others (Fig 6C).

Consistent with our findings for CNCCs and mesenchyme, gene ontology analysis revealed many biological processes, cellular component, and molecular process categories that were relevant for ectodermal subtypes (Figure S17). For example, markers for all three auditory subtypes were enriched for terms related to inner ear morphogenesis and development; genes biased for eye ectoderm were enriched for structural components of the lens; periderm marker genes were associated with the cornified envelope and skin development; markers for the thyroid cluster were enriched for thyroid hormone synthesis; and the markers of the pituitary were associated with pituitary gland development. The less specific clusters such as ectodermal surface clusters were enriched for a variety of categories suggesting they might be more regionally distinct cell states. In particular, surface3 marker genes were biased for oxidative phosphorylation and cytoplasmic translation compared to other ectodermal subtypes (Figure S17A-E). Examination of enriched human diseases revealed many tissue- or region-specific disorders including aniridia in the NaP cluster; nonsyndromic deafness in auditory clusters 1 and 2; thyroid agenesis for the thyroid cluster; anterior pituitary hypoplasia for the pituitary cluster; and congenital cataracts in the eye ectodermal cluster. Interestingly, median cleft lip and palate was only enriched in the pituitary cluster. Lastly marker genes of the ectodermal cluster expressing high levels of *EBF* genes (ect.EBF) were enriched for the largest number of disease categories suggesting this might be a particularly disease relevant cell type or state (Figure 6D).

Examination of overall ectodermal markers revealed relatively restricted expression to various surfaces in the human spatial transcriptomics data. One notable exception being OC90 that was strongly

expressed in the location of the putative inner ear (Fig. 6E). Subtype markers also showed generally restricted expression particularly for *DLX5, FOXE1,* and *SIX6*. *PITX2* was expressed in multiple putative fusion locations in the head but also strongly in the hindlimb (Fig. 6F). Markers of the ect.EBF subcluster, *EBF2* and *EBF3*, were biased in expression toward the head and pharyngeal arches of the CS13 human embryo. When we examined the spatial expression for both human CS13 and mouse E11.5, we found qualitatively different patterns of expression in the craniofacial regions corroborating our previous finding (Fig. S18). When we inspected module scores of each subtype, we observed exquisitely specific localization for some clusters like pituitary and auditory. Other clusters were generally enriched at surfaces of the pharyngeal arches and the putative esophagus (Fig. 6G).

Cell-type specific enrichment of genes and variants linked to orofacial abnormalities and normal facial variation.

The analysis above demonstrated strong concordance between human and mouse cell types and subtypes, showed coherent functional and disease enrichments across these cell types, and revealed spatial enrichments consistent with functions and expected anatomical locations. The strong support of our labelling of cell types across human craniofacial development, gave us the opportunity to interrogate the cell type-specific expression profiles for enrichment of craniofacial related genetic signals. The genetic contributions of common variants to many aspects of craniofacial variation have been studied in multiple populations based on frontal and profile photographs[87,88]. However, the cell types and embryonic landmarks that drive these differences are currently unknown. To address this issue, we first processed the genome-wide summary statistics[87,88] for each craniofacial landmark measurement with at least one genome-wide significant association using the linkage disequilibrium aware approach Multi-marker Analysis of GenoMic Annotation (MAGMA[89]. We then calculated expression weighted cell type enrichments[90] (EWCE) across all the cell types identified in our study using MAGMA-Celltyping[91]. We observed distinct patterns of cell type enrichment related to different sections of the face. We found that profile landmark measures related to soft tissues including multiple measures of lip thickness and shape, ear size, and nose shape were enriched primarily in ectodermal subtypes. Frontal landmark measures related to aspects of these same portions of the face such as the distance of the outer edge of the eye to the nasion (ExR-N) showed similar patterns of ectodermal enrichment. Measures likely to be influenced by bone or cartilage structure such as jaw, chin, and brow protrusion as well the positioning of the eyes relative to the base of the nose (EnL-Sn) and the mouth (ExR-ChR) were enriched primarily amongst mesenchymal subtypes (Fig. 7A). Amongst mesenchymal cell types, the mandibular arch, palatal shelf, and maxillary process fusion zone subclusters had largest number of significant enrichments for facial shape. The fusion zone cluster and surprisingly the pituitary cluster had the largest number of significant enrichments amongst ectodermal subtypes. Interestingly, while CNCCs certainly give rise to many of the downstream cell types and tissues, we found relatively few shape associations for CNCC subtypes. Overall, this analysis suggests specific cell subtypes contribute differentially to individual facial differences and suggest these effects begin to manifest very early in human development.

We next turned to studies of the genetic underpinnings of craniofacial abnormalities. In particular, there have been dozens of genetic associations identified for risk for orofacial clefting in multiple populations[92-106]. However, the cell types that potentially influence risk for clefting have not been

identified in human development. While orofacial clefting has been examined extensively using a variety of approaches, these studies have been performed in many different populations, making cross-study comparisons challenging [93,107-115]. Moreover, to identify true positive signals for cell type enrichments diseases that are not expected to be related to craniofacial cell types examined in the same population are needed as negative controls. To mitigate these issues, we turned to genome wide association studies that have been systematically performed on a large cohort of Finnish ancestry[116]. From this resource we selected all studies annotated as a congenital abnormality by FinnGen with at least one genome-wide significant association (n = 45) as well as two immune related diseases, Crohn's disease and systemic lupus erythematous (SLE), that we have used as negative controls in our previous studies[28,117]. When we analyzed these GWAS using the same approach as for facial variation we found similar partitioning of enrichment between specific classes of cell types (Fig 7B). We found that ectodermal cell subtypes were enriched for cleft lip with cleft palate (palate.surface), ankyloglossia, and other congenital malformation of the tongue and mouth (dental, fusion.zone). Mesenchymal subtypes were enriched for cleft lip or lip and palate (MxP_aLNP, mandibular arch 3, fusion mesenchyme subcluster 1 and 2), other congenital malformations of the ear (multiple palatal shelf subtypes), and congenital malformation of the musculoskeletal system (cartilage2) among others. CNCC subtypes were most consistently enriched for other congenital malformations of the upper alimentary tract. The immune cluster was most significantly enriched for Crohn's and SLE. Many other congenital abnormalities showed no significant enrichments for any craniofacial cell types demonstrating the specificity of our analyses. A few of these cell types, MxP_aLNP and ect_EBF in particular, were associated with both craniofacial disease and normal facial variation. These findings suggest that some cell types are contributors to both facial shape as well as risk for clefting. These results also point to underlying differences in how clefting phenotypes are categorized which are then in turn related to different subtypes of mesenchyme and ectoderm.

Our results from the marker gene ontology enrichments and common variant associations point to relevant craniofacial disease and phenotype enrichments for specific craniofacial cell types. However, it is unclear if these cell types might be generally informative for other human phenotypes. We posited that integrating continuous expression patterns instead of just binary marker gene identity may reveal additional associations. To address this, we employed a systematic examination of the entire Human Phenotype Ontology (HPO)[118,119] (Fig 7C). As expected, the immune cluster was systematically enriched for 90 of 253 phenotypes related to abnormality of the immune system. The red blood cell cluster was enriched for terms related to abnormality of metabolism and homeostasis (60 of 782 phenotypes). Both these cell types were enriched for phenotypes related to abnormalities of blood and blood-forming tissues (150 and 75 of 536 respectively). The endothelium cluster was enriched for abnormality of the cardiovascular system (60 of 672 phenotypes).

Amongst ectodermal subtypes we found the eye subcluster was strongly enriched for phenotypes related to abnormalities of the eye (75 of 717). Periderm, palate surface, and surface 2 and 3 subtypes were enriched for abnormalities of the integument. As expected, the pituitary and thyroid subtypes were associated with abnormalities of the endocrine system. Surprisingly many of the ectodermal subtypes were enriched for phenotypes related to abnormalities of the respiratory and genitourinary systems. Among the mesenchymal subclusters, many were enriched for abnormalities of the head and neck. The cartilage1 cluster showed the most diverse enrichments including phenotypes related to growth

abnormalities and abnormalities of the musculoskeletal system, ear, and limb. The main CNCC cluster was enriched for abnormalities of the nervous system, driven by most of the CNCC subclusters with the exception of the cnl1,3, and 4 subclusters. Surprisingly the specialized ectodermal subtype ect.GDNF was significantly associated with abnormalities of the voice. Together these results suggest that some subtypes we identified are not specific to the head and are more general states like cartilage. Moreover, this analysis revealed that while no major cell types were enriched for neoplasms, late CNCCs employ gene expression programs that likely trigger overgrowth.

Differential enrichment of curated gene lists revealed distinct disease risk and role in skull shape and/or function across hominid evolution.

Thus far our analysis of the craniofacial cell types has leveraged annotated ontology categories and common variant associations. Other gene lists that are not part of these systematic ontology databases and potentially of use to the craniofacial field have not been interrogated. To address this were assembled multiple gene lists relevant for orofacial clefting including those compiled by CleftGeneDB[120], genes co-expressed in important gene modules or prioritized for craniofacial disease in our recent work[13], and genes with distinct classes of *de novo* mutations (synonymous vs protein altering) in orofacial cleft trios sequenced as part of the Gabriella Miller Kids First program [121,122] and CPSeq Studies[123]. We also curated genes at the extremes of tolerance to loss of function mutations in otherwise healthy populations that have been suggested to be enriched or depleted of disease relevant genes[124]. Lastly given our findings for common facial variation across humans, we wondered whether genes potentially regulated by Neanderthal derived sequences might have craniofacial cell type specific enrichments. As a control for this evolutionary analysis, we included genes near human accelerated regions, which have been reported to be enriched in neuronal related functions and expression[125-128].

With these lists in hand, we again employed the expression weighted cell type enrichment approach. We found that the CleftGeneDB, craniofacial black co-expression modules, and our prioritized gene lists showed similar patterns of significant enrichments in mesenchymal subtypes including multiple clusters related to the maxillary process, palatal shelves, and lateral nasal process (Fig. 8A). Relatively few ectodermal and CNCC subtypes were enriched for these gene lists. The genes identified by gnomAD to have the least tolerance for loss of function mutations (LOUEF decile 1) were significantly enriched in many different subtypes identified by our analysis. In particular, MxP.aLNP cluster showed the most significant enrichment. This contrasted with those genes with the most tolerance for loss of function mutations (LOUEF decile 9) that showed few enrichments and were generally non-overlapping with the LOUEF decile 1 enrichments (Fig. 8A).

When we analyzed the genes near Neanderthal derived sequences, we found patterns of cell type enrichment distinct from the more disease-focused lists described above. The strongest enrichment was observed in pLNP2 mesenchyme subtype. We identified the specialized ect.EBF and ect.GDNF clusters, two fusion mesenchyme subtypes, and cartilage1. Interestingly all three auditory types were significantly enriched in this analysis. This was contrasted by only a single cell type identified when examining HAR associated genes, consistent with their previously published association with brain cell types and neuronal function [125-127]. We found no consistent, significant enrichments from any of our randomly selected gene lists across the cell types in questions. We also found no enrichments for the red blood

cells across any of these gene lists, and only the gnomAD unconstrained genes for the immune cell types (Fig. 8A).

We then turned to recently identified *de novo* variants from orofacial clefting trios from the Gabriella Miller Kids First program[121,122] and CPSeq studies[123]. We found no enrichment in any cell types for genes affected by *de novo* synonymous variants. We found no enrichment in any cell types for genes affected by *de novo* synonymous variants. However, we identified multiple cell types that strongly express genes with *de novo* protein altering variants (Fig. 8A). Palate ectoderm showed the strongest enrichment from this analysis, a cell type that was not enriched for any of the community curated gene lists related to clefting nor our previous prioritized genes[13]. Multiple other ectodermal cell types were also identified as enriched including multiple surface ectodermal subtypes, specialized ectoderm ect.EBF and ect.GDNF, fusion zone ectoderm, and the nasal placode (NaP). Fewer mesenchymal cell type enrichments were observed but identified the MxP.aLNP and others related the lateral nasal process (pLNP2, pLNP.fusion).

These findings suggest that current disease associations have been biased for genes expressed in the mesenchyme and that many genes expressed in ectodermal subtypes are also substantial contributors to clefting risk. To explore this concept further we wondered whether not only the number of genes, but the total number of *de novo* variants observed in genes might reveal additional disease associations. When we applied a computational framework that examines gene lists for excess *de novo* mutational load[129,130] we largely confirmed the findings from the EWCE analysis. We identified 22 clusters for which a least one phenotype was significantly enriched using a Benjamin-Hochberg false discovery rate of <10% (Fig. 8B and Supplemental Table 30). These included 17 for all trios with OFCs, 19 for trios with CLP, and 5 for trios with CP. We identified 14 significant enrichments across ectodermal cell types (n=22), 7 enrichments from mesenchymal cell types (n=22) and a single CNCC subtype (n=11). Only 3 clusters were significantly enriched in all three categories (NaP, palate, and cartilage1), whereas there were 12 shared between all OFCs and CL/P and 2 shared between all OFCs and CP. We also found 5 clusters that were only significant in the CL/P group and 1 that was only significant in the full cohort. No significant findings were observed for endothelium, muscle, red blood cell, or immune cell types in our data.

For the ectodermal subtypes we identified strongest enrichment *for de novo* variants identified in the whole cohort and those probands with cleft lip with cleft palate (CL/P) in the nasal placode, surface3, and palate.surface. We only identified significant enrichment *of de novo* variants from cleft palate only probands (CP) in the nasal placode and palate ectoderm. While fewer significant enrichments were observed for mesenchymal subtypes, we found cartilage1 was enriched for all analyses performed. Interestingly several subtypes were biased toward significant enrichment related to CP vs CL/P. For instance, MxP2 and palatal shelf 2.1 were enriched for the former while pLNP2 and pLNP.fusion for the latter (Fig.8B).

To explore the genes driving these enrichments we examined the genes with *de novo* damaging variants that were markers for the nasal placode, the most significantly enriched subtype across our analysis. As expected, these genes were all expressed in the NaP cells, but were frequently expressed in many other types of ectoderm to varying degrees (Fig. 8C). In particular, a high degree of sharing of expression was observed with periderm and multiple surface subtypes, including genes previously

implicated in orofacial clefting like *TP63*, *IRF6*, and *CDH1*. Among the *de novo* damaged genes those with the most biased expression in NaP were *SFRP4* and *DNAH11*. When we examined the localization of the NaP cells on the spatial transcriptomics data, we found discrete localization at the putative frontonasal and maxillary processes (Fig 8D). Finally, when we examined these genes for known disease enrichments, we found enrichment for various types of clefting and craniofacial abnormalities (Fig 8E). These were driven largely by the genes listed above related to clefting. Interestingly many of the genes we identified here are expressed in similar patterns to those known disease genes, but have not been associated with many human disease phenotypes. Amongst these *SFRP4* has the highest specificity of expression across the main cell types and ectodermal cell types (Fig 8E).

Compared to the shared expression and overlapping genes between the NaP and palate clusters, the genes driving enrichment in cartilage1 were more distinct. Interestingly, although both CP and CL/P were enriched to a similar degree, the makeup of genes contributing to this signal was different. For CP, the main driver of the signal was due to *COL2A1* variants, which made up half of the observed variants, where the remainder were single gene contributions (total n=10). This gene has fairly restricted expression in the head region and presumptive somites of the CS13 embryo (Figure S19). In contrast, CL/P probands collectively were enriched within cartilage1, but there were no genes that were individually overrepresented—only *KCNH5* had multiple variants (2 of total n=18), and the rest were a single variant per gene. This enrichment highlights the importance of these cells in OFC etiology, but the difference in signal drivers may provide insight into the heterogeneity of the genetic architecture between CP and CL/P.

Discussion

Craniofacial abnormalities are some of the most common human birth defects. Only recently have gene expression patterns active during human craniofacial development been examined[13] . We previously showed that genes specifically or co-expressed across craniofacial development relative to other tissues were enriched for known disease-causing genes[13]. However, these analyses relied on bulk gene expression data from the developing craniofacial tissues. The face is a complex structure that is derived from multiple cell lineages like ectoderm, mesenchyme, and the specialized neural crest. These major cell types undergo differentiation to become a variety of distinct cell types that make up the face including bone, cartilage, muscle, mucosa, and vasculature. Our bulk analyses showed strong bias for gene programs expressed in human and mouse mesenchyme preventing analysis of genes in ectodermal and other less abundant cell types. While other single cell atlases from human embryonic development have been described, there were few biological replicates and relatively few cells clearly derived from craniofacial regions[24-27]. Moreover, few craniofacial centric analyses have been previously performed on such data.

Our work here attempted to address these shortcomings and concentrate on cell types that are present across many of the major milestones of human craniofacial development. In this work we profiled multiple biological replicates from six distinct stages of human craniofacial development. Across these data we identified seven major cell types present in the developing human face. Most of these, including mesenchyme, ectoderm, endothelium, blood, and immune cells, have been previously identified in mouse craniofacial development[12-16]. However, we identified two distinct clusters not described in those

previous efforts or labelled as cell types not expected to exist in high levels in craniofacial tissues like glia or Schwann cells. Our thorough characterization of these clusters using curation of genes from the literature as well as extensive gene and disease ontology analyses point to these clusters being muscle progenitors and cranial neural crest. While several protocols for deriving neural crest like cells from human embryonic stem cells have been described, the primary CNCCs have remained elusive. Also, only a handful of well-known neural crest genes have been examined using immunohistochemistry in a small number of early human embryos[71]. Thus, it is unclear the complete repertoire of genes that are active in this cell type and how closely in vitro models reflect the primary gene expression patterns. Our analysis here not only established a large number of known marker genes as bona fide CNCC genes, including *FOXD3* and *SOX10*, but also identifies new genes that could be important for CNCC specification or function such as *INSC*, *ABCA8*, and *CTXND1*. Our identification of subclusters of the CNCC including putative melanocytes and the expression programs within them are likely to be useful to many researchers interested in these cell types. Moreover, identification of this exotic cell type and subtypes is not a fluke. Generation of data from mouse from similar tissues and stages and uniform process reveal these same populations. Upon close inspection of the gene ontology enrichments, other groups may have mistakenly labelled these cells as glia or Schwann cells simply because of biases in the ontology databases. Far more research has been performed on the human brain and related cell types than other parts of the body, likely resulting in many more brain related gene ontology annotations. While automated and machine learning based approaches are gaining traction for labelling of single cell atlases[131-137], transient developmentally related cell types that are not in current databases and biases in ontology will still require close inspection and interpretation.

By generating comparable datasets from both mouse and human we had the unique opportunity to identify both shared and species-biased gene programs active in individual cell types. As expected, we found the main cell types identified in each species share the most significant amount of marker genes with the orthologous cell type in the other species. Among these, mesenchyme was the most functionally shared between human and mouse based on marker gene expression. Surprisingly, CNCC markers were the least shared between these species, even less than cells from the immune system that has been documented to have substantial differences across humans and mice[17]. This could reflect substantial functional differences in CNCC between human and mice and indicate that this cell type may be particularly labile across evolution allowing innovation of craniofacial shape as others have proposed[1,18-20,70,138].

Although there was the largest degree of shared marker gene expression within mesenchyme, we found hundreds of differences in marker gene identity between human and mouse. While we restricted our analysis to genes with clear one-to-one orthology between these two species, some of these differences could be due to mis-annotation of orthology, substantial developmental heterochrony, or the inherit noisiness of current single nucleus gene expression data. However, by focusing on coherent gene ontologies and strongly expressed genes we identified many genes that are likely to reflect true species differences. For instance, one of the top human mesenchymal markers based on absolute and specificity of expression that was not revealed in mice was *ALX3*. Recessive mutations in human *ALX3* have been linked to frontorhiny or frontonasal dysplasia 1 (OMIM 136760)[139], while the *Alx3*$^{-/-}$ mouse has been reported to have no phenotype[140]. Our analysis also identified *MSX2,* to which humans have been

suggested to be much more sensitive than mice to dosage of this transcription factor during craniofacial development[141]. Further analysis of all these subtypes and comparison with additional species could reveal novel functional differences as well as the core regulatory programs that are present in all vertebrates.

While we highlighted some of the species differences in major cell types that could be relevant for what human genes and diseases can be modelled in mice, our comparison framework allowed us to accurately identify subtypes of each major cell types between species. This allowed us to leverage the substantial single-cell and spatial transcriptomics resources as well cell type annotations that have been generated by many different groups[23,86,142]. By transferring functional and spatial labels for mouse cell subtypes to our human data we could add such information to data that were originally lacking. We confirmed these labels using a variety of gene and disease ontology analyses, but most convincingly by leveraging previously published spatial transcriptomics data for a CS13 human embryo[25]By using marker genes to calculate module scores across this spatial data we confirmed relevant anatomical regions from which each subtype was potentially derived. We were able to identify some exquisitely specific spatial locations for ectodermal subtypes related to the ear, eye, and pituitary. We also identified expected regionalized expression for mesenchymal subtypes putatively derived from the mandibular arch as well as important fusion zones like the lateral nasal process. Further characterization of the markers we identified in higher resolution spatial transcriptomics across multiple sections and reconstruction into a complete three-dimensional representation as has been recently described for mice will be necessary to validate these findings[143].

One of the major goals of generating such resources is to enable better understanding of human phenotypes and disease. Not only can facial abnormalities affect our capacity for communication and feeding, but the face is also one of the most defining features of each human and is intimately tied to our sense of individuality. Thus, understanding how facial shape is encoded in our genomes is of substantial general interest. In recent years coupling of two- and three-dimensional imaging approaches with large scale genotyping has enabled the discovery of common genetic variants associated with quantitative differences in many different facial landmarks[87,88,144-146]. While these variants have been shown to be enriched in regulatory regions active in the developing face, the cell types that underly facial differences were unknown. Using our highly confident cell subtype annotations, we found distinct differences in enrichments for measurements across the human face. In general, the enrichments we observed were mutually exclusive, features likely driven by mesenchyme subtypes not associated with an ectodermal subtype and vice versa. As expected, mesenchyme subtypes were associated with features that are likely driven by hard structures like bone and cartilage while ectoderm subtypes were associated with some measures that are related to soft tissue shape or thickness. The most consistent associations observed were related to variation in measures of the midface. These were significantly enriched for many mesenchyme subtypes that we annotated as derived from regions that are consistent with these effects: the maxillary process, palatal shelves, and fusion zone mesenchyme. We did not observe any subtype that contributed to all aspects of the face, nor did we observe significant subtype enrichments for all measurements. These landmarks may be driven by cell types that appear later in development or be influenced by subtle gene expression differences in many cell subtypes. While the two studies we utilized were performed in populations with distinct ancestries and yielded consistent results, it is

762 possible that subtypes could influence facial variation differently in other populations. Further
763 identification of genetic associations with more facial measures in a more diverse set of individuals and
764 identification of cell types later in craniofacial development will be needed to address this issue.

765

766 Craniofacial abnormalities are among the most common birth defects in humans. The most common
767 form of these, nonsyndromic cleft lip and/or cleft palate, is thought to occur relatively early in human
768 development between 4 and 6 weeks[8,147,148]. Consistent with this idea, we found that variants associated
769 with risk for orofacial clefting are enriched in regulatory sequences active in craniofacial tissues from
770 this developmental window[28]. However, the cell types in which these variants manifest their effects were
771 unknown. Here we used uniformly generated and processed genome-wide association data for many
772 congenital abnormalities in the Finnish population. This population has been shown to have a high
773 incidence of clefting with interesting geographical distributions[149], and we reasoned would serve as an
774 excellent test case for subtype enrichments across relevant and unrelated diseases. Indeed, we found
775 some subtypes of both mesenchyme and ectoderm were significantly enriched for orofacial clefting or
776 other abnormalities of mouth. We found some overlap between phenotypes and subtypes particularly
777 related to cardiac outflow tract abnormalities consistent with the neural crest derived nature of those
778 structures[150-154]. We found expected cell type specific enrichments for immune cells in the autoimmune
779 related diseases that we included from this cohort, SLE and Crohn's. We also did not observe
780 enrichment for most subtypes in most abnormalities outside the craniofacial and cardiac structures.

781 Interestingly several of the enrichments we observed for subtypes were shared across the craniofacial
782 variation and craniofacial abnormality analyses. The MxP.aLNP and ect.EBF subtypes were examples
783 that had several significant associations in both phenotypes. This is particularly interesting as it has been
784 speculated that some of the same processes may be at play[102,155-158]. Our findings here suggest that some
785 cell types play an outsized role in landmarks of the midface region and risk for orofacial clefting. Our
786 analysis of marker genes for these specialized subtypes suggests these two subtypes are near one
787 another spatially and could be located near the fusion zone termed the "lambdoid junction"[86,159-161].
788 Failure of this region to fuse in humans has been suggested to cause cleft clip that could also involve the
789 nostril region and primary palate[10,147,162,163]. It is thus relatively straightforward to imagine that subtle
790 differences in the timing of migrations and fusion of cells residing in this region could influence the shape
791 of the midface. Interestingly, some of the major markers of the specialized ectodermal subtype are
792 multiple members of the EBF family of transcription factors. Our previous work suggested that these
793 genes were co-expressed more strongly in human craniofacial cell types than mouse, and found
794 compelling evidence that *EBF3* is a *bona fide* orofacial clefting risk gene[13]. This EBF family of
795 transcription factors have been linked to regulation of differentiation of multiple different tissue types
796 and predisposition for several tumor types[164-170]. The timing of differentiation of cells at a fusion zone
797 could influence the degree to which structures fuse and impact both clefting risk and facial shape.
798 Studies leveraging the marker genes we have identified for each of these subtypes could allow more
799 specific labelling and identification of these cells in human tissues and mouse embryos as well as
800 experiments to test impact of facial variation.

Our analysis of curated gene lists that are not included in standard gene ontologies was also revealing related to both the cell type identities as well as the composition of the gene lists themselves. For instance, our previous prioritized gene list as well as the curated CleftGeneDB resource are heavily biased toward some mesenchymal subtypes. This is not surprising given the ratios of cell types we observed in the data generated here. Mesenchyme is by far the dominant major cell type, thus previous studies of gene expression and protein expression from bulk tissues were heavily biased toward this cell type. The genes identified as constrained in human populations were more broadly enriched across all the cell subtypes suggesting they play critical roles in most cell types in the body. As expected, the unconstrained genes were enriched in relatively few cell types and were not enriched in the likely craniofacial disease relevant subtypes. While both the common variant analyses for orofacial clefting and the curated craniofacial disease gene lists were biased toward mesenchyme subtypes, genes harboring rare *de novo* protein damaging variants identified in cleft probands showed much more enrichment in ectodermal subtypes. This trend was not observed for *de novo* synonymous variants suggesting this was not a population specific effect or other artifacts of sequencing. This trend was further supported when we examined the frequency of *de novo* protein altering variants, where we found significant enrichment in multiple ectoderm subtypes primarily for CL/P. While the number of CP only cases were fewer than CL/P, we found these *de novo* variants were enriched in a few mesenchymal subtypes that make sense for a spatial perspective. Overall, this points to the ectodermal subtypes, that as we discussed above make up a small proportion of craniofacial tissue, as a major contributor to clefting risk. Due to the biases of previous studies for the most abundant cell types there are likely many additional clefting risk genes that remain to be discovered. The resources we described here could help further prioritize genes that are discovered in such sequencing cohorts. For instance, the nasal placode ectodermal subtype was marked the most substantial number of genes with *de novo* damaging variants. Many known disease risk genes are expressed in this subtype thus genes with similar patterns of expression or specificity of expression could be guilty by association. In particular, our analysis highlighted the *SFRP4* gene. This gene has been linked to Pyle disease (OMIM 265900) that features bone abnormalities and fragility particularly of the long bones and GWAS of bone mineral density[171-174]. Similar phenotypes are observed in *Sfrp4* knockout mice[175]. Cell type specific dysregulation of this gene either due to somatic mosaicism or regulatory element disruption could result in bone abnormalities or other defects in a relevant part of the developing face. Further studies of this gene in a craniofacial specific context in mice as well as identification of the regulatory landscape controlling could reveal a role in clefting risk.

As detailed above, our analysis of craniofacial variation revealed multiple cell types that contribute to human facial shape. Beyond interindividual differences there have been reported to be substantial differences in the shape of many craniofacial features between modern humans and of closely related but extinct hominid species such as Neanderthal and Denisovans[176-178] . Identifying the genetic contributions to these differences and if Neanderthal derived sequences in the human genome predispose individuals to specific phenotypes or diseases has been of particular interest[179-185]. While Neanderthal derived variants in genes and regulatory regions active in adult bulk tissues have been linked to specific phenotypes related to brain and cranium shape, immunity, and adipose function[186-189], it is unknown if any human developmental cell types might be influenced by such variants. Our analysis

points to Neanderthal derived regions in the European genetic background are systematically enriched near genes with biased expression in multiple cell types related to ear development, cartilage, and specialized ectodermal subtypes. Cartilage1 and EBF expressing ectodermal subtype (ect.EBF) were also shown to be enriched for both *de novo* protein damaging variants in orofacial clefting probands and several aspects of modern human facial variation. These results could suggest that risk for orofacial clefting and facial shape could both be influenced by Neanderthal introgression events. We did not observe any such enrichments for sequences that have been shown to be accelerated on the human lineage, suggesting that findings are functionally relevant. Consistent with this idea, the Neanderthal derived analysis was the only one that demonstrated enrichment in all the ear related ectodermal subtypes. Multiple aspects of Neanderthal inner ear morphology have been shown to differ substantially from modern humans and other primates[190,191]. We also note that we observed enrichment of Neanderthal introgressed regions near genes with biased expression in the specialized ectodermal subcluster ect.GDNF. This was the lone subtype that was enriched for abnormalities of the voice. Differential DNA methylation patterns between modern humans and Neanderthals and Denisovans indicated genes related to vocal anatomy are regulated in a distinct fashion[192]. Thes findings open the distinct possibility that the degree of introgressed segments in the genomes of modern human individuals could influence ear morphology and hearing capabilities as well as vocal characteristics.

In summary we have provided a substantial resource for understanding the cell types and gene expression patterns that build the human and mouse face. Our analyses revealed relationships between specific cell subtypes and many aspects of human biology including facial shape and orofacial clefting risk. We also illuminated potential contributions of ancient hominids to craniofacial morphology. Future integration with cell type specific chromatin accessibility could reveal specific variants and regulatory regions that encode such phenotypic differences, risk factors, and species-specific biology. This data can be explored through an interactive web application that is accessible to most researchers: https://cotneyshiny.research.chop.edu/shiny-apps/craniofacial_all_snRNA/. The data will be deposited to other major single cell aggregation databases including the Chan-Zuckerberg CellXGene Discover resource [39,193].

Acknowledgements

We would like to thank members of the UConn/JAXGM Single Cell Genomics Core for help with standardizing single-cell isolation techniques and preparing sequencing libraries. We would also like to thank members of the UConn Computational Biology Core and High-Performance Computing Facility for assistance with package installation and software/hardware support. We are grateful to Dr. Peter Tran, Dr. Sungryong Oh, and Pooja Sonawane for constructive feedback and copyediting. This work was funded by grants from the National Institutes of Health to E.J.L.C (R01-DE030342, X01-HG010835, X01-HD100701, X01-HL132363) and JC (NIDCR 1R01DE028945, NIDCR 1R03DE028588, and NIGMS 5R35GM119465).

Author contributions

Conceptualization: J.C. Investigation: N.F., E.W.W. and J.C. Formal analysis: N.F., E.W.W, B.M.S. K.R., S.W.C, J.C. Writing—original draft: J.C. Writing— review and editing: N.F., E.W.W, B.S, K.R., S.W.C, N.G.S, E.J.L.C., J.C. Funding acquisition: J.C. Supervision: J.C., E.J.L.C., S.G.K.

Code and data availability

Code for analysis and generation of figures can be found on github (https://github.com/cotneylab/craniofacial_snrna). An interactive website for exploring processed data is found here: https://cotneyshiny.research.chop.edu/shiny-apps/craniofacial_all_snRNA/. Raw data from mouse experiments generated in this work will be deposited in GEO. Cellranger ARC gene expression outputs for both human and mouse are available on Zenodo.

Methods

Human tissue samples

The use of human embryonic tissue was reviewed and approved by the Human Subjects Protection Program at UConn Health (UCHC 710-2-13-14-03) and Children's Hospital of Philadelphia (IRB 24-022258*)*. Human embryonic craniofacial tissues were collected via the Joint MRC/Wellcome Trust Human Developmental Biology Resource (HDBR) under-informed ethical consent with Research Tissue Bank ethical approval (18/LO/0822 and 18/NE/0290, project 200225). Donations of tissue to HDBR are made entirely voluntarily by women undergoing termination of pregnancy. Donors are asked to give explicit written consent for the fetal material to be collected, and only after they have been counseled about the termination of their pregnancy. Further documentation of all policies and ethical approvals for HDBR sample collection can be found at https://www.hdbr.org/ethical-approvals. Tissues were flash-frozen upon collection and stored at −80 °C. Upon thawing, the samples were quickly inspected for intactness of the general craniofacial prominences and processed for single nucleus multiomics.

Mouse embryonic tissue samples

The use of mouse embryonic tissues was reviewed and approved by the UConn Health Institutional Animal Care and Use Committee (Protocol AP-2000061-0723). Eight-week-old wild-type male and female C57BL6/J mice were obtained from Jackson Laboratory. Mice were housed according to recommendations by Jackson Laboratory with 12 h light:dark cycle beginning at 7 a.m. The ambient temperature was maintained between 20 and 22 °C and humidity was maintained at 40–60%. Mice were given ad libitum access to food and water. Timed matings were established by the identification of vaginal plugs the morning following the housing of a single male with multiple female mice. Embryos were harvested from pregnant mothers at mid-day either 10, 11, or 12 days after identification of the vaginal plug. The staging was confirmed by counting somites and comparing overall morphology to the Theiler Staging Criteria[194]. All embryos from a given litter were combined for individual biological replicates, and at least three biological replicates were collected and processed for each stage. Craniofacial prominences were collected in a very similar fashion to human samples and subsequently prepared for single nucleus multiomics.

Single nucleus multiomics

Primary human craniofacial tissues from CS12, CS13, CS14, CS16, CS17 and CS20, each stage represented by a minimum of 3 replicates, were obtained from HDBR. Tissue from each embryo were mechanically broken into single-cell suspensions and cells were checked for viability counted using Trypan blue staining following the 10X Genomics protocol for single-cell multiome sequencing using the ChromiumX controller. Samples were sequenced on multiple Illumina NovaSeq runs according to 10X Genomics recommendations. Raw fastqs were processed using CellRanger ARC (v2.0.2) using hg38 genome and gene annotations provided by 10X Genomics.

Primary mouse craniofacial tissues from E10.5-E12.5 from multiple (3-5 depending on stage) mixed sex C57BL/6J Mus Musculus embryos (Jackson Laboratories) were pooled. Animals were raised and sacrificed in compliance with UConn Health IACUC approval (protocol AP-200061-0723). Samples were mechanically broken into single-cell suspensions, processed for multiome using the ChromiumX controller, and sequenced in the same fashion as for human samples above. Raw fastqs were processed using CellRanger ARC (v2.0.2) using mm10 genome and gene annotations provided by 10X Genomics.

Processing of snRNA and identification of major cell types.

Filtered barcode matrices from each human samples generated by CellRanger ARC were individually loaded with Read10X_h5 command in Seurat[195] and merged into one object. Percentage of mitochondrial reads were calculated for each cell and filtering was performed to only retain cells with less than ten percent mitochondrial derived. Further filtering was performed based on number of counts per cell ($500 < x < 25000$) and number of genes detected per cell ($500 < x < 7000$). Filtered data were normalized with default values and cell cycle scores were calculated using Seurat. Data was scaled based on S and G2M score regression and dimensionality reduction with principal component analysis (PCA) were performed using respective commands in Seurat. The top 2000 variable features were identified and data were then further integrated with harmony R package[196]. Nearest neighbors based on harmony corrected embeddings were calculated with up to 30 dimensions and clusters were identified with multiple resolutions from 0.1 to 1 in Seurat. We then performed uniform manifold approximation and projection (UMAP) dimensionality reduction using harmony corrected embeddings in Seurat (dimensions = 30, minimum distance = 0.3). Resulting clusters were inspected for expression of multiple craniofacial markers form Li et al 2019 and marker genes were identified for each cluster. Cells from clusters identified with high expression of neuronal markers *TUBB3* and *MAP2* were removed and the process of normalization, harmonization, and clustering was repeated with remaining cells from all samples. Marker genes for major cell types were identified using FindAllMarkers (logfc.threshold = 0.25, min.pct = 0.1, test.use = “wilcox”, min.cells.feature = 3, mi.cells.group = 3, pseudocount.use =1, and return.thresh = 0.01). The top 100 marker genes for each cluster ($p < 0.05$, ranked by log2fold change versus all other clusters) were then analyzed for gene and disease ontology enrichments using compareCluster in clusterProfiler R package (v. 4.12.6). Cranial neural crest genes were compiled based on markers identified by regulatory network construction in human cultured CNCC and craniofacial tissue data[69]. Major cell type labels were applied to each cluster.

For mouse data sets, filtered barcode matrices from each mouse E10.5 to 12.5 samples generated by CellRanger ARC were individually loaded with Read10X_h5 command in Seurat[195] and merged with E13.5 to E15.5 data from Pina et al 2023 (GSE205448). Calculation of percent mitochondrial reads and filtering were performed with similar thresholds to human data above. Subsequent harmonization, dimensionality reduction, and clustering were performed identically to those for human data above. Less significant contamination of neuronal cell types was observed in mouse data, which was identified and filtered as describe for human. Identification of marker genes and gene ontology enrichments, and CNCC modules scores were performed as above for human data. Major cell type labels were applied to each mouse cluster.

Marker gene comparisons across species

Lists of all marker genes for each of the seven main subtypes for each species ($p < 0.05$) were compiled and orthology based on HGNC symbol annotated by Ensembl v105 was obtained using the getLDS command in the biomaRt R package (v. 2.60.1). Only genes that had one ortholog in each species and a HGNC symbol were retained (n = 7504). Significant overlaps between all orthologous marker gene lists were determined using the testGeneOverlap command in GeneOverlap R package[197] Conserved and species-specific genes were determined based on HGNC symbol and the intersection matrix obtained by getMatrix in GeneOverlap. Gene and disease ontology enrichments were calculated using clusterProfiler.

Final Seurat objects were prepared for display in an interactive webapp using the ShinyCell R Package[198].

Subclustering of major cell types

For major cell types labelled as mesenchymal, ectodermal, or CNCC further subclustering was first performed on mouse data. For each major cell type, normalization, scaling with regressed cell cycle impacts, harmonization, and subclusters were identified using same procedure as described above. Marker genes were identified for each cluster and functional enrichments were determined using clusterProfiler. Annotations for each cluster were manually assigned based on those originally described[12-16]. Mouse cell subtype assignments were further confirmed with ToppGene[199] using the scToppR package[200]. Mouse main and subtype annotations were further confirmed by projection on mouse E15.5 spatial transcriptomics data[23] (GSE245469). Links between snRNA and spatial data were determined using FindTransferAnchors and transferred using TransferData in Seurat.

Following annotation of subtypes and for comparison with human data, an intermediate data set was created where mouse genes were reduced and converted to those to those with one to one orthology with human genes using annotations provided by Ensembl (archive dec2021) with biomaRt R package[201]. The intermediate dataset was used to transfer mouse subtype annotations to human subtypes by first identifying shared features across clusters using FindTransferAnchors in Seurat with log normalization and canonical correlation analysis (cca). Predicted subtype labels were transferred to human subtypes using TransferData in Seurat and further confirmed with a confusion matrix. Marker genes for human subtypes were identified as performed for major cell types and functional enrichments were characterized with compareCluster in clusterProfiler. Final Seurat main objects and subtype objects were prepared for display in an interactive webapp using the ShinyCell R Package[198]. Seurat objects were also converted to scanpy and anndata objects using scEasy R package (v0.0.7) for hosting at the Chan Zuckerberg CELL by GENE Discover resource.

997

998 *Processing of spatial transcriptomics*

999 Spatial transcriptomics data for two sections of a human CS13 embryo[25] were retrieved from
1000 https://heoa.shinyapps.io/code/. Raw sequence count matrices were loaded using the Read10x command of
1001 Seurat[195] and converted to HDF5 format. These counts were then combined with spot coordinates and section
1002 images using CreateSeuratObject. Data from both slices were merged and variable features were determined
1003 using Seurat. The percentage of mitochondrial reads was determined for each cell and was used to transform
1004 all data in the merged object using SCTransform from Seurat. Data was clustered using UMAP and plotted
1005 which revealed a strong batch effect between the two spatial objects. Data was further normalized using
1006 Harmony (v1.2.3), projected using UMAP, and clustered with a resolution of 0.8. Marker genes for the 22
1007 clusters were identified using FindAllMarkers in Seurat. The top 100 marker genes for each cluster ($p < 0.05$,
1008 ranked by log2fold change versus all other clusters) were then analyzed for gene and disease ontology
1009 enrichments using compareCluster in clusterProfiler R package (v. 4.12.6). Enrichments and spatial
1010 localization were compared to previous annotations by Xu et al 2023 and labelled accordingly. The top 100
1011 marker genes from each of the subclusters identified in human craniofacial data were used to calculate
1012 module scores across the merged spatial object and plotted using SpatialFeaturePlot in Seurat.
1013
1014 We chose mouse E11.5 spatial transcriptomics data as it is most morphologically similar to CS13 human
1015 embryos. Data were retrieved all E11.5 spatial transcriptomics data from the MOSTA resource[43] and loaded
1016 into Seurat as for human data above. For each section, module scores of top 100 marker genes for each main
1017 cluster or subcluster were calculated. Gene spatial feature plots for selected genes and module scores were
1018 then generated with Seurat.
1019

1020 *Facial variation and congenital abnormality GWAS enrichments*

1021 We retrieved summary statistics for facial variation[87,88] and all congenital abnormality GWAS summary
1022 statistics from FinnGenn[116]. Raw summary stats were further processed and standardized with hg38
1023 cooridinates with MungeSumstats R package (https://doi.org/10.1093/bioinformatics/btab665). Variants were
1024 mapped to genes +/- 100kb using MAGMA[89]Frontal facial measures and FinnGenn were processed based on
1025 1000 genome European population while profile facial measures were processed with the 1000 genome
1026 Middle/South American population all obtained from the MAGMA website (https://cncr.nl/research/magma/).
1027 We converted the Seurat snRNA-seq expression data to a CellTypeData set with the Expression Weighted
1028 Celltype Enrichment (EWCE) R package[90] and then assessed each study trait for a linear positive correlation of
1029 cell type gene expression specificity and gene-level genetic associations using MAGMA Celltyping[91]. Plots
1030 were generated using tidyheatmaps in R[202].
1031

1032 *Gene list enrichments per cell type*

1033 The CellTypeData-formatted human craniofacial snRNA-seq objects were generated using
1034 generate_celltype_data in EWCE (v1.15.0). Mean and specificity metrics for several marker genes (*SOX10*,
1035 *TP63*, and *MSX1*) were inspected across main cell types and subtypes using plot_ctd in EWCE. Gene lists were
1036 compiled from multiple resources including gnomAD (v4.1), CleftGeneDB, prioritized genes and black module

from craniofacial WGCNA[13], and genes affected *by de novo* variation in orofacial clefting probands[32,123]. For Neanderthal introgressed regions and human accelerated regions, coordinates were obtained from respective publications[188,203] and assigned single nearest gene using rGREAT[204] with "oneClosest" association rule. Each gene list was then tested for linear association using bootstrap enrichment test in EWCE (reps = 10,000; geneSizeControl = TRUE). Results from all gene lists were then merged and plotted with ewce_plot in EWCE with correction for total number of gene lists and cell types tested using the Benjamini-Hochberg approach.

Phenotype-cell type association tests

To map the relationships between cell types and phenotypes, we ran pairwise association tests between all combinations of cell types in our snRNA-seq-derived CellTypeData and phenotypes across the Human Phenotype Ontology (HPO)[119] using the run_phenomix function from MSTExplorer (v1.0.5). In contrast to the gene list-based approaches (e.g. EWCE) this function reframes the problem as a series of linear regressions by leveraging continuous scores that summarize the current strength of evidence for a causal relationship between each gene-phenotype pair (using additional data from the Gene Curation Coalition)[118,205]. The continuous nature of this data allows us to more accurately capture phenotype-cell type relationships, especially for phenotypes with large gene lists where only some genes have strong evidence of actually causing the phenotype. The gene signature vectors for each phenotype were previously merged and shared as a single precomputed gene (5003 unique gene symbols) x phenotype (11047 unique HPO phenotypes) association matrix. Next, a series of linear regressions tests were performed between the gene specificity vectors of each cell type (n=66 vectors) and the gene association vectors of each phenotype (n=11047 vectors). Finally, multiple-testing correction was applied using Benjamini-Hochberg False Discovery Rate[206] (at FDR<5% significance).

For the purposes of summarization and visualization, the number of significantly associated phenotypes per cell type were then computed within each major HPO branch (Fig. 7C). Here, we define HPO branches as groups of related phenotypes that can be labeled according to their shared ancestral term, e.g., 'Abnormality of the immune system'. Next, we sought to determine whether some cell types were disproportionately more often associated with phenotypes of a particular HPO branch. To accomplish this, we performed a series of proportion tests comparing the proportion of total phenotypes that a given cell type was significantly associated with within a target HPO branches relative to all other HPO branches. In practice, we computed 2x2 contingency tables (number of significant phenotype association vs. number of non-significant phenotype associations x target branch vs. non-target branches) for each cell type within each HPO branch, which were then used as inputs to the prop_test function within the rstatix R package (v0.7.2). This test appropriately takes into account the different number of phenotypes across HPO branches. Only one-sided tests were performed to test whether the target HPO branch was greater than all other (non-target) branches (set with the alternative = "greater" parameter). All proportion tests were then corrected for multiple testing at FDR<5%.

Orofacial Clefting de novo variant analysis

We used the R package 'DenovolyzeR' (version 0.2.0) to test enrichment of *de novo* variants (DNs) in a dataset of OFC case-parent trios. Enrichment is calculated by comparing the expected number of variants, as determined by mutation models described by Samocha, et al[130], to the observed number of

variants in a given gene or group of genes using the 'DenovolyzeByClass' and 'includeGenes' functions. Using our dataset of 2031 DNs in 1171 genes identified in 1676 trios with OFCs, we first compared this list of genes to those with calculated mutational rates in the R package 'DenovolyzeR' (version 0.2.0) using the 'viewProbabilityTable()' function. There were 12 trios in which DNs were identified, but no mutational rates for the affected genes were present; thus, we ultimately tested 1662 trios with OFCs, broken down by subtype including 1180 cleft lip with or without cleft palate (CL/P; 226 cleft lip (CL), 954 cleft lip and palate (CLP)), and 482 cleft palate (CP) trios. We then tested enrichment of all OFC trios and by subtype within the top 20% of genes by log2FC derived from single nucleus RNA sequencing of human craniofacial tissue at CS20.

Figure Legends

Figure 1. Generation of single nucleus gene expression atlas of human craniofacial development.

A). Anatomical regions of the developing craniofacial region from 4 to 8 weeks post conception. Individual Carnegie Stages (CS) and replicates at stage are indicated below images. B). Pseudo-bulk gene expression of tissues from each stage displayed in principal component (PC) space based on the first two PCs. Progression of developmental time is indicated along PC1 dimension. C) UMAP projection and cluster identification of all human craniofacial cells after filtering of neurons. D). Number of cells obtained at each CS stage for each cluster identified in C. E). Distribution of samples from each sample across the UMAP projection.

Figure 2. Identification of main cell types in the developing human face.

A). Gene expression feature plots for indicated genes across UMAP projection. B) Average and percent expression for the top 10 maker genes for each main cluster. C). Disease ontology enrichments of categories curated by DisGeNet for each indicated cluster. D). Identification of CNCC cluster based on module score of curated neural crest genes and labelling of all remaining clusters. Violin plots and individual values for all cells of a given cluster type based on CNCC module score calculated by Seurat.

Figure 3. Identification of CNCC subtypes in the developing human face.

A). UMAP projection of subclustered CNCC main cell type. B). Contribution of cells from each CS timepoint to each CNCC subcluster. C) Violin plots of published neural crest marker genes across each subcluster. D). Average and percent expression for the top 5 marker genes for each of the CNCC subclusters. E). Gene expression spatial feature plot for indicated CNCC marker genes in two sections from a CS13 human embryo. F). Gene expression spatial feature plot for indicated CNCC subtype marker genes in same sections as E. G). Spatial feature plot for modules scores calculated from top 100 marker genes from indicated CNCC subtype.

Figure 4. Single-nucleus gene expression in the developing mouse face.

A). UMAP projection of all cells profiled by this study and combined with published studies. Major cell types are indicated. B) Heatmap of expression for indicated marker genes across each cluster. C). Spatial prediction of major cell types across E15.5 craniofacial section from Pina et al 2023[23]. D). Heatmap of sharing of marker genes between each major cell type in human and mouse. (P-values calculated by GeneOverlap R package). E). Network plot of human specific mesenchymal markers related to selected ontology categories. Shading of individual gene nodes based on fold change in expression of cells in the mesenchymal main cell type versus all other cell types. F). UMAP projection of subclustered CNCC cells from mouse. G). Gene ontology enrichments for indicated categories across each CNCC subcluster. H). Violin gene expression plots across CNCC subcluster for neural crest gene orthologous to human genes plotted in Fig. 3C. I). Average and percent expression for the top 5 marker genes for each of the mouse CNCC subclusters. J). UMAP projection of subclustered mesenchymal cells from mouse. K). Average and percent expression for the top 5 marker genes for each of the mouse mesenchymal subclusters. L). Spatial feature plot for module scores of top 100 marker genes of the PalatalShelf2 subcluster on a section of a mouse E11.5 embryo[43]. M). UMAP projection of subclustered ectodermal cells from mouse. N). Average and percent expression for the top 5 marker genes for each of the mouse ectodermal subclusters. O). Spatial feature plot for module scores of top 100 marker genes of the palate surface subcluster on a section of a mouse E11.5 embryo[43]. P). Spatial predictions of selected craniofacial subtypes on E15.5 craniofacial section from Pina et al 2023[23].

Figure 5. Identification of mesenchymal subtypes in human craniofacial development.

A). UMAP projection of subclustered mesenchymal main cell type. Subtype labels based on transfer of mouse mesenchymal subtypes to human. B). Contribution of cells from each CS timepoint to each mesenchymal subcluster. C) Average and percent expression for the top 5 marker genes for each of the mesenchymal subclusters. D). Disease ontology enrichments for each of the indicated mesenchymal subcluster. E.) Gene expression spatial feature plot for indicated mesenchymal marker genes in two sections from a CS13 human embryo. F). Gene expression spatial feature plot for indicated mesenchymal subtype marker genes in same sections as E. G). Spatial feature plot for modules scores calculated from top 100 marker genes from indicated mesenchymal subtype.

Figure 6. Identification of ectodermal subtypes in human craniofacial development.

A). UMAP projection of subclustered ectodermal main cell type. Subtype labels based on transfer of mouse ectodermal subtypes to human. B). Contribution of cells from each CS timepoint to each ectodermal subcluster. C) Average and percent expression for the top 5 marker genes for each of the ectodermal subclusters. D). Disease ontology enrichments for each of the indicated ectodermal subcluster. E.) Gene expression spatial feature plot for indicated ectodermal marker genes in two sections from a CS13 human embryo. F). Gene expression spatial feature plot for indicated ectodermal subtype marker genes in same sections as E. G). Spatial feature plot for modules scores calculated from top 100 marker genes from indicated ectodermal subtype.

Figure 7. Enrichment of common variation associate with facial shape differences and congenital abnormality risk.

A). Clustered heatmap of significance values calculated by MAGMA Celltyping[91] for each facial variation trait and cell subtype. Profile landmark diagram adapted from Bonfante et al 2021[88]. Frontal landmark diagram adapted from Xiong et al 2019[87]. Colors along top of heatmap indicate main cell type classification. Shaded gray indicators along left of heatmap indicate study origin. Colors along left of heatmap indicate general region of the face each landmark is located. Hyphenated trait measures are obtained from Xiong et al 2019 and combinatorial code is indicated in coded legend (e.g., EnL-AIL indicates landmark segment 5 to 7). Descriptive named traits obtained from Bonfante et al 2021[88]. Levels of significance indicated by asterisks or period according to figure. B). Clustered heatmap of significance values calculated by MAGMA Celltyping[91] for each congenital abnormality or disease and cell subtype. Colors along top of heatmap indicate main cell type classification. Levels of significance indicated by asterisks or period according to figure. C) Barplot showing the number of enriched human phenotypes (max-normalized from 0-1 within each branch) for main cell types and subtypes as calculated by MSTExplorer::run_phenomix. Significance of the proportion tests, testing for disproportionate numbers of phenotype enrichments for a given cell type within a given HPO branch, is denoted with asterisks (FDR<0.001=***, FDR<0.01=**, FDR<0.05=*) as well as black outlines around the bars.

Figure 8. Genes associated with orofacial clefting, constraint in human populations, and Neanderthal introgression show distinct cell subtype enrichments.

A). Bar plot of standard deviations from the mean of bootstrapping tests performed by EWCE method[90] for each indicated gene list and cell subtype. Asterisks indicate significant subtype enrichments corrected for number of gene lists and cell subtypes performed for entire figure. B). Bubbleplot of -log10 transformed significance and fold enrichment values for each cell subtype from denovolzeR[129] analysis of protein *damaging de novo* variation in orofacial cleft trios from the Gabriella Miller Kids First program[121,122]. Colored circles indicate variants identified in whole cohort (Any), in cleft lip with cleft palate probands (CL/P), or cleft palate only probands (CP). Cell subtypes are clustered by main cell type. C) Average and percent expression across all ectodermal subtypes of genes identified in nasal placode subtype *with de novo* protein damaging mutations for B. D). Spatial feature plot of modules scores calculated from top 100 marker genes from nasal placode ectodermal subtype on

CS13 human embryo. E). Heatmap of fold differences in expression of each indicated gene in nasal placode subtype versus all other ectodermal cells. Presence or absence of box indicates membership in indicated disease ontology category indicated as significantly enriched in nasal placode marker genes.

References

1. Minoux, M. & Rijli, F.M. Molecular mechanisms of cranial neural crest cell migration and patterning in craniofacial development. *Development* **137**, 2605-2621 (2010).
2. Cordero, D.R. *et al.* Cranial neural crest cells on the move: Their roles in craniofacial development. *American Journal of Medical Genetics Part A* **155**, 270-279 (2011).
3. Tang, W. & Bronner, M.E. Neural crest lineage analysis: from past to future trajectory. *Development* **147**(2020).
4. Guo, J. *et al.* Variation and signatures of selection on the human face. *J Hum Evol* **75**, 143-52 (2014).
5. Mitteroecker, P., Gunz, P., Bernhard, M., Schaefer, K. & Bookstein, F.L. Comparison of cranial ontogenetic trajectories among great apes and humans. *J Hum Evol* **46**, 679-97 (2004).
6. Naqvi, S. *et al.* Decoding the Human Face: Progress and Challenges in Understanding the Genetics of Craniofacial Morphology. *Annu Rev Genomics Hum Genet* **23**, 383-412 (2022).
7. Smith, D.W. Recognizable patterns of human malformation: genetic, embryologic, and clinical aspects. *Major Probl Clin Pediatr* **7**, 1-368 (1970).
8. Leslie, E.J. & Marazita, M.L. Genetics of cleft lip and cleft palate. *American journal of medical genetics. Part C, Seminars in medical genetics* **163C**, 246-258 (2013).
9. Mc Goldrick, N. *et al.* A multi-program analysis of cleft lip with cleft palate prevalence and mortality using data from 22 International Clearinghouse for Birth Defects Surveillance and Research programs, 1974–2014. *Birth Defects Research* **115**, 980-997 (2023).
10. Mossey, P.A., Little, J., Munger, R.G., Dixon, M.J. & Shaw, W.C. Cleft lip and palate. *Lancet* **374**, 1773-85 (2009).
11. Mai, C.T. *et al.* National population‐based estimates for major birth defects, 2010‐2014. *Birth defects research* **111**, 1420-1435 (2019).
12. Li, M. *et al.* Integrative functional genomic analysis of human brain development and neuropsychiatric risks. *Science (New York, NY)* **362**, eaat7615 (2018).
13. Yankee, T.N. *et al.* Integrative analysis of transcriptome dynamics during human craniofacial development identifies candidate disease genes. *Nat Commun* **14**, 4623 (2023).
14. Rajderkar, S.S. *et al.* Dynamic enhancer landscapes in human craniofacial development. *Nat Commun* **15**, 2030 (2024).
15. Sun, J. *et al.* Single-cell RNA-Seq reveals transcriptional regulatory networks directing the development of mouse maxillary prominence. *J Genet Genomics* **50**, 676-687 (2023).
16. Han, X. *et al.* Runx2-Twist1 interaction coordinates cranial neural crest guidance of soft palate myogenesis. *Elife* **10**(2021).
17. Mestas, J. & Hughes, C.C. Of mice and not men: differences between mouse and human immunology. *J Immunol* **172**, 2731-8 (2004).
18. Martik, M.L. & Bronner, M.E. Riding the crest to get a head: neural crest evolution in vertebrates. *Nat Rev Neurosci* **22**, 616-626 (2021).
19. York, J.R., Yuan, T. & McCauley, D.W. Evolutionary and Developmental Associations of Neural Crest and Placodes in the Vertebrate Head: Insights From Jawless Vertebrates. *Frontiers in Physiology* **11**(2020).
20. Donoghue, P.C.J., Graham, A. & Kelsh, R.N. The origin and evolution of the neural crest. *BioEssays* **30**, 530-541 (2008).

21. Selleri, L. & Rijli, F.M. Shaping faces: genetic and epigenetic control of craniofacial morphogenesis. *Nature Reviews Genetics* **24**, 610-626 (2023).
22. Martínez-Abadías, N. *et al.* The Developmental Basis of Quantitative Craniofacial Variation in Humans and Mice. *Evolutionary Biology* **39**, 554-567 (2012).
23. Pina, J.O. *et al.* Multimodal spatiotemporal transcriptomic resolution of embryonic palate osteogenesis. *Nat Commun* **14**, 5687 (2023).
24. Cao, J. *et al.* A human cell atlas of fetal gene expression. *Science* **370**(2020).
25. Xu, Y. *et al.* A single-cell transcriptome atlas profiles early organogenesis in human embryos. *Nature Cell Biology* **25**, 604-615 (2023).
26. Wang, C. *et al.* Single-cell RNA sequencing analysis of human embryos from the late Carnegie to fetal development. *Cell & Bioscience* **14**, 118 (2024).
27. Zeng, B. *et al.* The single-cell and spatial transcriptional landscape of human gastrulation and early brain development. *Cell Stem Cell* **30**, 851-866.e7 (2023).
28. Wilderman, A., VanOudenhove, J., Kron, J., Noonan, J.P. & Cotney, J. High-Resolution Epigenomic Atlas of Human Embryonic Craniofacial Development. *Cell Rep* **23**, 1581-1597 (2018).
29. Vieille-Grosjean, I., Hunt, P., Gulisano, M., Boncinelli, E. & Thorogood, P. Branchial HOX Gene Expression and Human Craniofacial Development. *Developmental Biology* **183**, 49-60 (1997).
30. Cai, J. *et al.* Gene expression in pharyngeal arch 1 during human embryonic development. *Hum.Mol.Genet.* **14**, 903-912 (2005).
31. Samuels, B.D. *et al.* FaceBase 3: analytical tools and FAIR resources for craniofacial and dental research. *Development (Cambridge)* **147**(2020).
32. Bishop, M.R. *et al.* Genome-wide Enrichment of De Novo Coding Mutations in Orofacial Cleft Trios. *American journal of human genetics* **107**, 124-136 (2020).
33. Schoenwolf, G.C., Bleyl, S.B., Brauer, P.R. & Francis-West, P. *Larsen's Human Embryology*, (Elsevier, Philadelphia, PA, 2021).
34. Jirasek, J.E. *An Atlas of Human Prenatal Developmental Mechanics: Anatomy and Staging*, 312 (CRC Press, London, 2004).
35. Brunskill, E.W. *et al.* A gene expression atlas of early craniofacial development. *Developmental biology* **391**, 133-146 (2014).
36. Hooper, J.E., Jones, K.L., Smith, F.J., Williams, T. & Li, H. An Alternative Splicing Program for Mouse Craniofacial Development. *Front Physiol* **11**, 1099 (2020).
37. Feng, W. *et al.* Spatial and temporal analysis of gene expression during growth and fusion of the mouse facial prominences. *PLoS One* **4**, e8066 (2009).
38. Hooper, J.E. *et al.* Systems biology of facial development: contributions of ectoderm and mesenchyme. *Developmental biology* **426**, 97-114 (2017).
39. Program, C.S.-C.B. *et al.* CZ CELL×GENE Discover: A single-cell data platform for scalable exploration, analysis and modeling of aggregated data. *bioRxiv*, 2023.10.30.563174 (2023).
40. Leland, M., Healy, J. & Melville, J. UMAP: Uniform Manifold Approximation and Projection for Dimension Reduction. *arXiv* **1802.03426**(2020).
41. Martin, J.F., Bradley, A. & Olson, E.N. The paired-like homeo box gene MHox is required for early events of skeletogenesis in multiple lineages. *Genes Dev* **9**, 1237-49 (1995).
42. Bartoletti, G., Dong, C., Umar, M. & He, F. Pdgfra regulates multipotent cell differentiation towards chondrocytes via inhibiting Wnt9a/beta-catenin pathway during chondrocranial cartilage development. *Developmental Biology* **466**, 36-46 (2020).
43. Chen, A. *et al.* Spatiotemporal transcriptomic atlas of mouse organogenesis using DNA nanoball-patterned arrays. *Cell* **185**, 1777-1792.e21 (2022).
44. Nikolopoulou, E. *et al.* Spinal neural tube closure depends on regulation of surface ectoderm identity and biomechanics by Grhl2. *Nature Communications* **10**, 2487 (2019).

45. Bebee, T.W. *et al*. The splicing regulators Esrp1 and Esrp2 direct an epithelial splicing program essential for mammalian development. *Elife* **4**(2015).
46. Revil, T. & Jerome-Majewska, L.A. During Embryogenesis, Esrp1 Expression Is Restricted to a Subset of Epithelial Cells and Is Associated With Splicing of a Number of Developmentally Important Genes. *Developmental Dynamics* **242**, 281-290 (2013).
47. Knowles, W.J., Bologna, M.L., Chasis, J.A., Marchesi, S.L. & Marchesi, V.T. Common structural polymorphisms in human erythrocyte spectrin. *J Clin Invest* **73**, 973-9 (1984).
48. Bennett, V. & Stenbuck, P.J. The membrane attachment protein for spectrin is associated with band 3 in human erythrocyte membranes. *Nature* **280**, 468-73 (1979).
49. Gardner, L.C., Smith, S.J. & Cox, T.M. Biosynthesis of delta-aminolevulinic acid and the regulation of heme formation by immature erythroid cells in man. *J Biol Chem* **266**, 22010-8 (1991).
50. Huang, C.H. The human Rh50 glycoprotein gene. Structural organization and associated splicing defect resulting in Rh(null) disease. *J Biol Chem* **273**, 2207-13 (1998).
51. Vallese, F. *et al*. Architecture of the human erythrocyte ankyrin-1 complex. *Nat Struct Mol Biol* **29**, 706-718 (2022).
52. Millauer, B. *et al*. High affinity VEGF binding and developmental expression suggest Flk-1 as a major regulator of vasculogenesis and angiogenesis. *Cell* **72**, 835-46 (1993).
53. Kendall, R.L., Wang, G. & Thomas, K.A. Identification of a natural soluble form of the vascular endothelial growth factor receptor, FLT-1, and its heterodimerization with KDR. *Biochem Biophys Res Commun* **226**, 324-8 (1996).
54. Justement, L.B., Campbell, K.S., Chien, N.C. & Cambier, J.C. Regulation of B cell antigen receptor signal transduction and phosphorylation by CD45. *Science* **252**, 1839-42 (1991).
55. Engel, P. *et al*. The B7-2 (B70) costimulatory molecule expressed by monocytes and activated B lymphocytes is the CD86 differentiation antigen. *Blood* **84**, 1402-7 (1994).
56. Wang, M.H. *et al*. Identification of the ron gene product as the receptor for the human macrophage stimulating protein. *Science* **266**, 117-9 (1994).
57. Weintraub, H. *et al*. The myoD gene family: nodal point during specification of the muscle cell lineage. *Science* **251**, 761-6 (1991).
58. Seidel, U. & Arnold, H.H. Identification of the functional promoter regions in the human gene encoding the myosin alkali light chains MLC1 and MLC3 of fast skeletal muscle. *J Biol Chem* **264**, 16109-17 (1989).
59. Karsch-Mizrachi, I., Travis, M., Blau, H. & Leinwand, L.A. Expression and DNA sequence analysis of a human embryonic skeletal muscle myosin heavy chain gene. *Nucleic Acids Res* **17**, 6167-79 (1989).
60. Takahashi, M. & Osumi, N. Identification of a novel type II classical cadherin: Rat cadherin19 is expressed in the cranial ganglia and Schwann cell precursors during development. *Developmental Dynamics* **232**, 200-208 (2005).
61. Izaki, T., Kamakura, S., Kohjima, M. & Sumimoto, H. Two forms of human Inscuteable-related protein that links Par3 to the Pins homologues LGN and AGS3. *Biochemical and Biophysical Research Communications* **341**, 1001-1006 (2006).
62. Puente, X.S., Pendás, A.M., Llano, E., Velasco, G. & López-Otín, C. Molecular cloning of a novel membrane-type matrix metalloproteinase from a human breast carcinoma. *Cancer Res* **56**, 944-9 (1996).
63. Sasai, N., Mizuseki, K. & Sasai, Y. Requirement of FoxD3-class signaling for neural crest determination in Xenopus. *Development* **128**, 2525-2536 (2001).
64. Kos, R., Reedy, M.V., Johnson, R.L. & Erickson, C.A. The winged-helix transcription factor FoxD3 is important for establishing the neural crest lineage and repressing melanogenesis in avian embryos. *Development* **128**, 1467-1479 (2001).

65. Lukoseviciute, M. *et al*. From Pioneer to Repressor: Bimodal foxd3 Activity Dynamically Remodels Neural Crest Regulatory Landscape In Vivo. *Developmental Cell* **47**, 608-628.e6 (2018).
66. Simões-Costa, M.S., McKeown, S.J., Tan-Cabugao, J., Sauka-Spengler, T. & Bronner, M.E. Dynamic and Differential Regulation of Stem Cell Factor FoxD3 in the Neural Crest Is Encrypted in the Genome. *PLOS Genetics* **8**, e1003142 (2012).
67. Simões-Costa, M. & Bronner, M.E. Establishing neural crest identity: a gene regulatory recipe. *Development (Cambridge)* **142**, 242-257 (2015).
68. Tirosh, I. *et al*. Dissecting the multicellular ecosystem of metastatic melanoma by single-cell RNA-seq. *Science* **352**, 189-96 (2016).
69. Feng, Z. *et al*. hReg-CNCC reconstructs a regulatory network in human cranial neural crest cells and annotates variants in a developmental context. *Communications Biology* **4**, 442 (2021).
70. Thomas, S. *et al*. Human neural crest cells display molecular and phenotypic hallmarks of stem cells. *Human Molecular Genetics* **17**, 3411-3425 (2008).
71. Betters, E., Liu, Y., Kjaeldgaard, A., Sundström, E. & García-Castro, M.I. Analysis of early human neural crest development. *Dev Biol* **344**, 578-92 (2010).
72. O'Rahilly, R. & Müller, F. The development of the neural crest in the human. *Journal of Anatomy* **211**, 335-351 (2007).
73. Rada-Iglesias, A. *et al*. Epigenomic annotation of enhancers predicts transcriptional regulators of human neural crest; PMC3751405. *Cell Stem Cell* **11**, 633-648 (2012).
74. Sun, K.Y. *et al*. A deep catalogue of protein-coding variation in 983,578 individuals. *Nature* (2024).
75. Aoto, K., Nishimura, T., Eto, K. & Motoyama, J. Mouse GLI3 Regulates Fgf8 Expression and Apoptosis in the Developing Neural Tube, Face, and Limb Bud. *Developmental Biology* **251**, 320-332 (2002).
76. Baker, J.L., Wood, B., Karpinski, B.A., LaMantia, A.S. & Maynard, T.M. Testicular receptor 2, Nr2c1, is associated with stem cells in the developing olfactory epithelium and other cranial sensory and skeletal structures. *Gene Expr Patterns* **20**, 71-9 (2016).
77. Mansouri, A., Hallonet, M. & Gruss, P. Pax genes and their roles in cell differentiation and development. *Curr Opin Cell Biol* **8**, 851-7 (1996).
78. Nakashima, K. *et al*. The Novel Zinc Finger-Containing Transcription Factor Osterix Is Required for Osteoblast Differentiation and Bone Formation. *Cell* **108**, 17-29 (2002).
79. Hojo, H., Ohba, S., He, X., Lai, L.P. & McMahon, A.P. Sp7/Osterix Is Restricted to Bone-Forming Vertebrates where It Acts as a Dlx Co-factor in Osteoblast Specification. *Dev Cell* **37**, 238-53 (2016).
80. Sur, A. *et al*. Single-cell analysis of shared signatures and transcriptional diversity during zebrafish development. *Dev Cell* **58**, 3028-3047.e12 (2023).
81. Van Otterloo, E. *et al*. AP-2α and AP-2β cooperatively function in the craniofacial surface ectoderm to regulate chromatin and gene expression dynamics during facial development. *Elife* **11**(2022).
82. De Felice, M. *et al*. A mouse model for hereditary thyroid dysgenesis and cleft palate. *Nat Genet* **19**, 395-8 (1998).
83. Sheng, H.Z. *et al*. Specification of pituitary cell lineages by the LIM homeobox gene Lhx3. *Science* **272**, 1004-7 (1996).
84. Raetzman, L.T., Ward, R. & Camper, S.A. Lhx4 and Prop1 are required for cell survival and expansion of the pituitary primordia. *Development* **129**, 4229-39 (2002).
85. Pina, J.O. *et al*. Spatial Multiomics Reveal the Role of Wnt Modulator, Dkk2, in Palatogenesis. *bioRxiv* (2024).
86. Li, H., Jones, K.L., Hooper, J.E. & Williams, T. The molecular anatomy of mammalian upper lip and primary palate fusion at single cell resolution. *Development (Cambridge)* **146**(2019).

87. Xiong, Z. *et al.* Novel genetic loci affecting facial shape variation in humans. *eLife* **8**, e49898 (2019).
88. Bonfante, B. *et al.* A GWAS in Latin Americans identifies novel face shape loci, implicating VPS13B and a Denisovan introgressed region in facial variation. *Science advances* **7**, eabc6160 (2021).
89. de Leeuw, C.A., Mooij, J.M., Heskes, T. & Posthuma, D. MAGMA: generalized gene-set analysis of GWAS data. *PLoS Comput Biol* **11**, e1004219 (2015).
90. Skene, N.G. & Grant, S.G. Identification of Vulnerable Cell Types in Major Brain Disorders Using Single Cell Transcriptomes and Expression Weighted Cell Type Enrichment. *Front Neurosci* **10**, 16 (2016).
91. Skene, N.G. *et al.* Genetic identification of brain cell types underlying schizophrenia. *Nature Genetics* **50**, 825-833 (2018).
92. Ludwig, K.U. *et al.* Imputation of Orofacial Clefting Data Identifies Novel Risk Loci and Sheds Light on the Genetic Background of Cleft Lip ± Cleft Palate and Cleft Palate Only. *Human Molecular Genetics* **26**, 829-842 (2017).
93. Leslie, E.J. *et al.* Association studies of low-frequency coding variants in nonsyndromic cleft lip with or without cleft palate. *American journal of medical genetics Part A* **100**, 493-8 (2017).
94. Butali, A. *et al.* Genomic analyses in African populations identify novel risk loci for cleft palate. *Hum Mol Genet* **28**, 1038-1051 (2019).
95. Huang, L. *et al.* Genetic factors define CPO and CLO subtypes of nonsyndromicorofacial cleft. *PLoS Genet* **15**, e1008357 (2019).
96. Leslie, E.J. *et al.* A multi-ethnic genome-wide association study identifies novel loci for non-syndromic cleft lip with or without cleft palate on 2p24.2, 17q23 and 19q13. *Human molecular genetics* **25**, 2862-2872 (2016).
97. He, M. *et al.* Genome-wide Analyses Identify a Novel Risk Locus for Nonsyndromic Cleft Palate. *J Dent Res* **99**, 1461-1468 (2020).
98. Curtis, S.W. *et al.* The PAX1 locus at 20p11 is a potential genetic modifier for bilateral cleft lip. *HGG Adv* **2**(2021).
99. Yu, Y. *et al.* Genome-wide analyses of non-syndromic cleft lip with palate identify 14 novel loci and genetic heterogeneity. *Nat Commun* **8**, 14364 (2017).
100. Wu, T. *et al.* Evidence of gene-environment interaction for two genes on chromosome 4 and environmental tobacco smoke in controlling the risk of nonsyndromic cleft palate. *PLoS One* **9**, e88088 (2014).
101. Sun, Y. *et al.* Genome-wide association study identifies a new susceptibility locus for cleft lip with or without a cleft palate. *Nat Commun* **6**, 6414 (2015).
102. Howe, L.J. *et al.* Investigating the shared genetics of non-syndromic cleft lip/palate and facial morphology. *PLoS Genet* **14**, e1007501 (2018).
103. Ray, D. *et al.* Pleiotropy method reveals genetic overlap between orofacial clefts at multiple novel loci from GWAS of multi-ethnic trios. *PLoS Genet* **17**, e1009584 (2021).
104. Curtis, S.W. *et al.* FAT4 identified as a potential modifier of orofacial cleft laterality. *Genet Epidemiol* **45**, 721-735 (2021).
105. Haaland Ø, A. *et al.* A genome-wide scan of cleft lip triads identifies parent-of-origin interaction effects between ANK3 and maternal smoking, and between ARHGEF10 and alcohol consumption. *F1000Res* **8**, 960 (2019).
106. Carlson, J.C. *et al.* Genome-wide interaction studies identify sex-specific risk alleles for nonsyndromic orofacial clefts. *Genet Epidemiol* **42**, 664-672 (2018).
107. Grosen, D. *et al.* Risk of oral clefts in twins. *Epidemiology (Cambridge, Mass.)* **22**, 313-319 (2011).
108. Christensen, K. & Andersen, P.F. Isolated Cleft Palate in Danish Multiple Births, 1970-1990. *The Cleft Palate Craniofacial Journal* **30**, 469-474 (1993).

109. Christensen, K. The 20th century Danish facial cleft population--epidemiological and genetic-epidemiological studies. *Cleft Palate Craniofac J* **36**, 96-104 (1999).
110. Diaz Perez, K.K. *et al.* Rare variants found in clinical gene panels illuminate the genetic and allelic architecture of orofacial clefting. *Genetics in Medicine* **25**(2023).
111. Auslander, A. *et al.* The International Family Study of Nonsyndromic Orofacial Clefts: Design and Methods. *The Cleft Palate Craniofacial Journal* **59**, S37-S47 (2021).
112. Marazita, M.L. *et al.* Meta-Analysis of 13 Genome Scans Reveals Multiple Cleft Lip/Palate Genes with Novel Loci on 9q21 and 2q32-35. *The American Journal of Human Genetics* **75**, 161-173 (2004).
113. Ludwig, K.U. *et al.* Genome-wide meta-analyses of nonsyndromic cleft lip with or without cleft palate identify six new risk loci. *Nature genetics* **44**, 968-971 (2012).
114. Ludwig, K.U. *et al.* Meta-analysis Reveals Genome-Wide Significance at 15q13 for Nonsyndromic Clefting of Both the Lip and the Palate, and Functional Analyses Implicate GREM1 As a Plausible Causative Gene. *PLoS Genetics* **12**, e1005914 (2016).
115. Yu, Y. *et al.* Genome-wide meta-analyses identify five new risk loci for nonsyndromic orofacial clefts in the Chinese Han population. *Molecular Genetics & Genomic Medicine* **11**, e2226 (2023).
116. Kurki, M.I. *et al.* FinnGen provides genetic insights from a well-phenotyped isolated population. *Nature* **613**, 508-518 (2023).
117. VanOudenhove, J., Yankee, T., Wilderman, A. & Cotney, J. Epigenomic and Transcriptomic Dynamics During Human Heart Organogenesis. *Circulation research* **127**, e184-e209 (2020).
118. Murphy, K.B. *et al.* Identification of cell type-specific gene targets underlying thousands of rare diseases and subtraits. *medRxiv*, 2023.02.13.23285820 (2023).
119. Gargano, M.A. *et al.* The Human Phenotype Ontology in 2024: phenotypes around the world. *Nucleic Acids Research* **52**, D1333-D1346 (2023).
120. Xu, H. *et al.* CleftGeneDB: a resource for annotating genes associated with cleft lip and cleft palate. *Science bulletin* **66**, 2340-2342 (2021).
121. Mukhopadhyay, N. *et al.* Whole genome sequencing of orofacial cleft trios from the Gabriella Miller Kids First Pediatric Research Consortium identifies a new locus on chromosome 21. *Human Genetics* **139**, 215-226 (2020).
122. Curtis, S.W. *et al.* Rare genetic variants in SEC24D modify orofacial cleft phenotypes. *medRxiv* (2023).
123. Robinson, K. *et al.* Trio-based GWAS identifies novel associations and subtype-specific risk factors for cleft palate. *medRxiv*, 2023.03.01.23286642 (2023).
124. Karczewski, K.J. *et al.* The mutational constraint spectrum quantified from variation in 141,456 humans. *Nature* **581**, 434-443 (2020).
125. Doan, R.N. *et al.* Mutations in Human Accelerated Regions Disrupt Cognition and Social Behavior. *Cell* **167**, 1-27 (2016).
126. Levchenko, A., Kanapin, A., Samsonova, A. & Gainetdinov, R.R. Human Accelerated Regions and Other Human-Specific Sequence Variations in the Context of Evolution and Their Relevance for Brain Development. *Genome Biol Evol* **10**, 166-188 (2018).
127. Driessens, S.L.W. *et al.* Genes associated with cognitive ability and HAR show overlapping expression patterns in human cortical neuron types. *Nature Communications* **14**, 4188 (2023).
128. Prabhakar, S. *et al.* Human-Specific Gain of Function in a Developmental Enhancer. *Science (New York, NY)* **321**, 1346-1350 (2008).
129. Ware, J.S., Samocha, K.E., Homsy, J. & Daly, M.J. Interpreting de novo Variation in Human Disease Using denovolyzeR. *Curr Protoc Hum Genet* **87**, 7.25.1-7.25.15 (2015).
130. Samocha, K.E. *et al.* A framework for the interpretation of de novo mutation in human disease. *Nat Genet* **46**, 944-50 (2014).

131. Luecken, M.D. *et al.* Benchmarking atlas-level data integration in single-cell genomics. *Nature Methods* **19**, 41-50 (2022).
132. Luecken, M.D. & Theis, F.J. Current best practices in single‐cell RNA‐seq analysis: a tutorial. *Molecular Systems Biology* **15**, e8746 (2019).
133. Heumos, L. *et al.* Best practices for single-cell analysis across modalities. *Nature Reviews Genetics* **24**, 550-572 (2023).
134. Amezquita, R.A. *et al.* Orchestrating single-cell analysis with Bioconductor. *Nature Methods* **17**, 137-145 (2020).
135. Abdelaal, T. *et al.* A comparison of automatic cell identification methods for single-cell RNA sequencing data. *Genome Biology* **20**, 194 (2019).
136. Domínguez Conde, C. *et al.* Cross-tissue immune cell analysis reveals tissue-specific features in humans. *Science* **376**, eabl5197 (2022).
137. Fischer, F. *et al.* scTab: Scaling cross-tissue single-cell annotation models. *Nature Communications* **15**, 6611 (2024).
138. Prescott, Sara L. *et al.* Enhancer Divergence and cis-Regulatory Evolution in the Human and Chimp Neural Crest. *Cell* **163**, 68-83 (2015).
139. Twigg, S.R. *et al.* Frontorhiny, a distinctive presentation of frontonasal dysplasia caused by recessive mutations in the ALX3 homeobox gene. *Am J Hum Genet* **84**, 698-705 (2009).
140. Beverdam, A., Brouwer, A., Reijnen, M., Korving, J. & Meijlink, F. Severe nasal clefting and abnormal embryonic apoptosis in Alx3/Alx4 double mutant mice. *Development* **128**, 3975-86 (2001).
141. Wilkie, A.O. *et al.* Functional haploinsufficiency of the human homeobox gene MSX2 causes defects in skull ossification. *Nat Genet* **24**, 387-90 (2000).
142. Ye, Q., Bhojwani, A. & Hu, J.K. Understanding the development of oral epithelial organs through single cell transcriptomic analysis. *Development* **149**(2022).
143. Qiu, X. *et al.* Spatiotemporal modeling of molecular holograms. *Cell*.
144. Weinberg, S.M., Cornell, R. & Leslie, E.J. Craniofacial genetics: Where have we been and where are we going? *PLoS Genet* **14**, e1007438 (2018).
145. Claes, P. *et al.* Genome-wide mapping of global-to-local genetic effects on human facial shape. *Nat Genet* **50**, 414-423 (2018).
146. White, J.D. *et al.* Insights into the genetic architecture of the human face. *Nat Genet* **53**, 45-53 (2021).
147. Dixon, M.J., Marazita, M.L., Beaty, T.H. & Murray, J.C. Cleft lip and palate: understanding genetic and environmental influences. *Nature reviews Genetics* **12**, 167-178 (2011).
148. Marazita, M.L. The evolution of human genetic studies of cleft lip and cleft palate. *Annual Review of Genomics and Human Genetics* **13**, 263-283 (2012).
149. Rahimov, F. *et al.* High incidence and geographic distribution of cleft palate in Finland are associated with the IRF6 gene. *Nat Commun* **15**, 9568 (2024).
150. Kirby, M.L. & Waldo, K.L. Role of neural crest in congenital heart disease. *Circulation* **82**, 332-340 (1990).
151. Farrell, M., Waldo, K., Li, Y.-X. & Kirby, M.L. A Novel Role for Cardiac Neural Crest in Heart Development. *Trends in Cardiovascular Medicine* **9**, 214-220 (1999).
152. Bronner, M.E. Formation and migration of neural crest cells in the vertebrate embryo. *Histochemistry and Cell Biology* **138**, 179-186 (2012).
153. Etchevers, H.C., Dupin, E. & Le Douarin, N.M. The diverse neural crest: from embryology to human pathology. *Development* **146**(2019).
154. Yamagishi, H. Cardiac Neural Crest. *Cold Spring Harbor Perspectives in Biology* **13**(2021).
155. Rahimov, F. *et al.* Disruption of an AP-2alpha binding site in an IRF6 enhancer is associated with cleft lip. *Nature genetics* **40**, 1341-1347 (2008).

156. Indencleef, K. *et al*. Six NSCL/P Loci Show Associations With Normal-Range Craniofacial Variation. *Frontiers in Genetics* **9**(2018).
157. Indencleef, K. *et al*. The Intersection of the Genetic Architectures of Orofacial Clefts and Normal Facial Variation. *Frontiers in Genetics* **12**(2021).
158. Weinberg, S.M. What's Shape Got to Do With It? Examining the Relationship Between Facial Shape and Orofacial Clefting. *Frontiers in Genetics* **13**(2022).
159. Tamarin, A. & Boyde, A. Facial and visceral arch development in the mouse embryo: a study by scanning electron microscopy. *J Anat* **124**, 563-80 (1977).
160. Depew, M.J. & Compagnucci, C. Tweaking the hinge and caps: testing a model of the organization of jaws. *J Exp Zool B Mol Dev Evol* **310**, 315-35 (2008).
161. Losa, M. *et al*. Face morphogenesis is promoted by Pbx-dependent EMT via regulation of Snail1 during frontonasal prominence fusion. *Development* **145**(2018).
162. Jiang, R., Bush, J.O. & Lidral, A.C. Development of the upper lip: morphogenetic and molecular mechanisms. *Dev Dyn* **235**, 1152-66 (2006).
163. Wang, K.H. *et al*. Evaluation and integration of disparate classification systems for clefts of the lip. *Front Physiol* **5**, 163 (2014).
164. Lin, H. & Grosschedl, R. Failure of B-cell differentiation in mice lacking the transcription factor EBF. *Nature* **376**, 263-7 (1995).
165. Jin, S. *et al*. Ebf factors and MyoD cooperate to regulate muscle relaxation via Atp2a1. *Nature communications* **5**, 3793 (2014).
166. Garcia-Dominguez, M., Poquet, C., Garel, S. & Charnay, P. Ebf gene function is required for coupling neuronal differentiation and cell cycle exit. *Development* **130**, 6013-25 (2003).
167. Parsons, D.W. *et al*. An integrated genomic analysis of human glioblastoma multiforme. *Science* **321**, 1807-12 (2008).
168. Jones, D.L. & Wagers, A.J. No place like home: anatomy and function of the stem cell niche. *Nat Rev Mol Cell Biol* **9**, 11-21 (2008).
169. Zardo, G. *et al*. Integrated genomic and epigenomic analyses pinpoint biallelic gene inactivation in tumors. *Nature Genetics* **32**, 453-458 (2002).
170. Liao, D. Emerging roles of the EBF family of transcription factors in tumor suppression. *Mol Cancer Res* **7**, 1893-901 (2009).
171. Cho, Y.S. *et al*. A large-scale genome-wide association study of Asian populations uncovers genetic factors influencing eight quantitative traits. *Nat Genet* **41**, 527-34 (2009).
172. Kiel, D.P. *et al*. Genome-wide association with bone mass and geometry in the Framingham Heart Study. *BMC Med Genet* **8 Suppl 1**, S14 (2007).
173. Koller, D.L. *et al*. Genome-wide association study of bone mineral density in premenopausal European-American women and replication in African-American women. *J Clin Endocrinol Metab* **95**, 1802-9 (2010).
174. Styrkarsdottir, U. *et al*. Multiple genetic loci for bone mineral density and fractures. *N Engl J Med* **358**, 2355-65 (2008).
175. Kiper, P.O.S. *et al*. Cortical-Bone Fragility--Insights from sFRP4 Deficiency in Pyle's Disease. *N Engl J Med* **374**, 2553-2562 (2016).
176. Bilsborough, A. Cranial Morphology of Neanderthal Man. *Nature* **237**, 351-352 (1972).
177. MORANT, G.M. STUDIES OF PALAEOLITHIC MAN. *Annals of Eugenics* **2**, 318-381 (1927).
178. Falk, D. Comparative anatomy of the larynx in man and the chimpanzee: Implications for language in Neanderthal. *American Journal of Physical Anthropology* **43**, 123-132 (1975).
179. Prüfer, K. *et al*. The complete genome sequence of a Neanderthal from the Altai Mountains. *Nature* **505**, 43-9 (2014).
180. Noonan, J.P. Neanderthal genomics and the evolution of modern humans. *Genome research* **20**, 547-553 (2010).

181. Noonan, J.P. *et al.* Sequencing and analysis of Neanderthal genomic DNA. *Science* **314**, 1113-8 (2006).
182. Sankararaman, S., Patterson, N., Li, H., Pääbo, S. & Reich, D. The date of interbreeding between Neandertals and modern humans. *PLoS genetics* **8**, e1002947 (2012).
183. Moorjani, P. *et al.* A genetic method for dating ancient genomes provides a direct estimate of human generation interval in the last 45,000 years. *Proceedings of the National Academy of Sciences* **113**, 5652-5657 (2016).
184. Green, R.E. *et al.* A draft sequence of the Neandertal genome. *Science (New York, NY)* **328**, 710-722 (2010).
185. Vernot, B. *et al.* Excavating Neandertal and Denisovan DNA from the genomes of Melanesian individuals. *Science* **352**, 235-239 (2016).
186. van Galen, P. *et al.* Reduced Lymphoid Lineage Priming Promotes Human Hematopoietic Stem Cell Expansion. *Cell Stem Cell* **14**, 94-106 (2014).
187. Telis, N., Aguilar, R. & Harris, K. Selection against archaic hominin genetic variation in regulatory regions. *Nature Ecology & Evolution* **4**, 1558-1566 (2020).
188. McArthur, E., Rinker, D.C. & Capra, J.A. Quantifying the contribution of Neanderthal introgression to the heritability of complex traits. *Nature Communications* **12**, 4481 (2021).
189. Gregory, M.D. *et al.* Neanderthal-Derived Genetic Variation Shapes Modern Human Cranium and Brain. *Scientific Reports* **7**, 6308 (2017).
190. Stoessel, A. *et al.* Morphology and function of Neandertal and modern human ear ossicles. *Proc Natl Acad Sci U S A* **113**, 11489-11494 (2016).
191. Spoor, F., Hublin, J.J., Braun, M. & Zonneveld, F. The bony labyrinth of Neanderthals. *J Hum Evol* **44**, 141-65 (2003).
192. Gokhman, D. *et al.* Differential DNA methylation of vocal and facial anatomy genes in modern humans. *Nat Commun* **11**, 1189 (2020).
193. Megill, C. *et al.* cellxgene: a performant, scalable exploration platform for high dimensional sparse matrices. *bioRxiv*, 2021.04.05.438318 (2021).
194. Theiler, K. *The House Mouse : Atlas of Embryonic Development*, (Springer Science+Business Media, 1989).
195. Hao, Y. *et al.* Dictionary learning for integrative, multimodal and scalable single-cell analysis. *Nature Biotechnology* **42**, 293-304 (2024).
196. Korsunsky, I. *et al.* Fast, sensitive and accurate integration of single-cell data with Harmony. *Nature Methods* **16**, 1289-1296 (2019).
197. Shen, L.S.I. GeneOverlap: Test and visualize gene overlaps. (2024).
198. Ouyang, J.F., Kamaraj, U.S., Cao, E.Y. & Rackham, O.J.L. ShinyCell: simple and sharable visualization of single-cell gene expression data. *Bioinformatics* **37**, 3374-3376 (2021).
199. Chen, J., Bardes, E.E., Aronow, B.J. & Jegga, A.G. ToppGene Suite for gene list enrichment analysis and candidate gene prioritization. *Nucleic Acids Research* **37**, W305-W311 (2009).
200. Granger, B. & Berto, S. scToppR: a coding-friendly R interface to ToppGene. *Bioinformatics* **40**(2024).
201. Durinck, S. *et al.* BioMart and Bioconductor: a powerful link between biological databases and microarray data analysis. *Bioinformatics* **21**, 3439-3440 (2005).
202. Engler, J. tidyheatmaps: Heatmaps from Tidy Data. (2024).
203. Keough, K.C. *et al.* Three-dimensional genome rewiring in loci with human accelerated regions. *Science* **380**, eabm1696 (2023).
204. Gu, Z. & Hübschmann, D. rGREAT: an R/bioconductor package for functional enrichment on genomic regions. *Bioinformatics* **39**(2023).
205. DiStefano, M.T. *et al.* The Gene Curation Coalition: A global effort to harmonize gene-disease evidence resources. *Genet Med* **24**, 1732-1742 (2022).

206. Benjamini, Y. & Hochberg, Y. Controlling the False Discovery Rate - a Practical and Powerful Approach to Multiple Testing. *Journal of the Royal Statistical Society Series B-Methodological* **57**, 289-300 (1995).

A

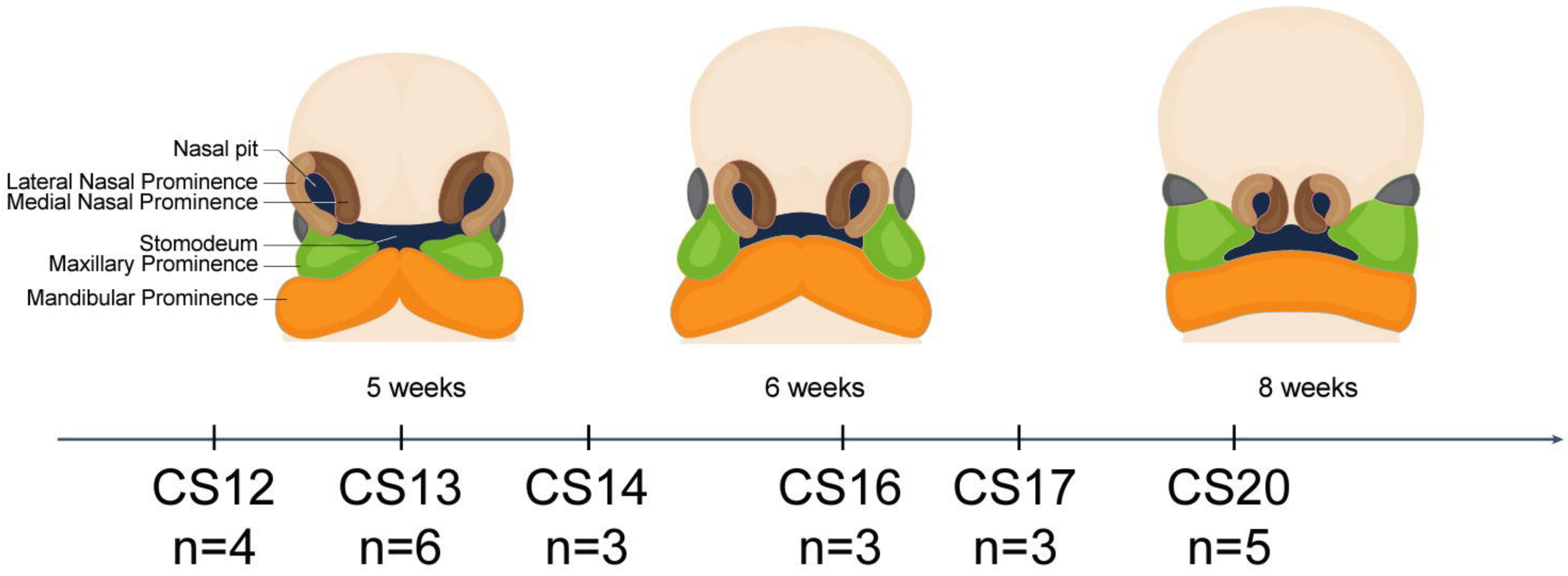

B

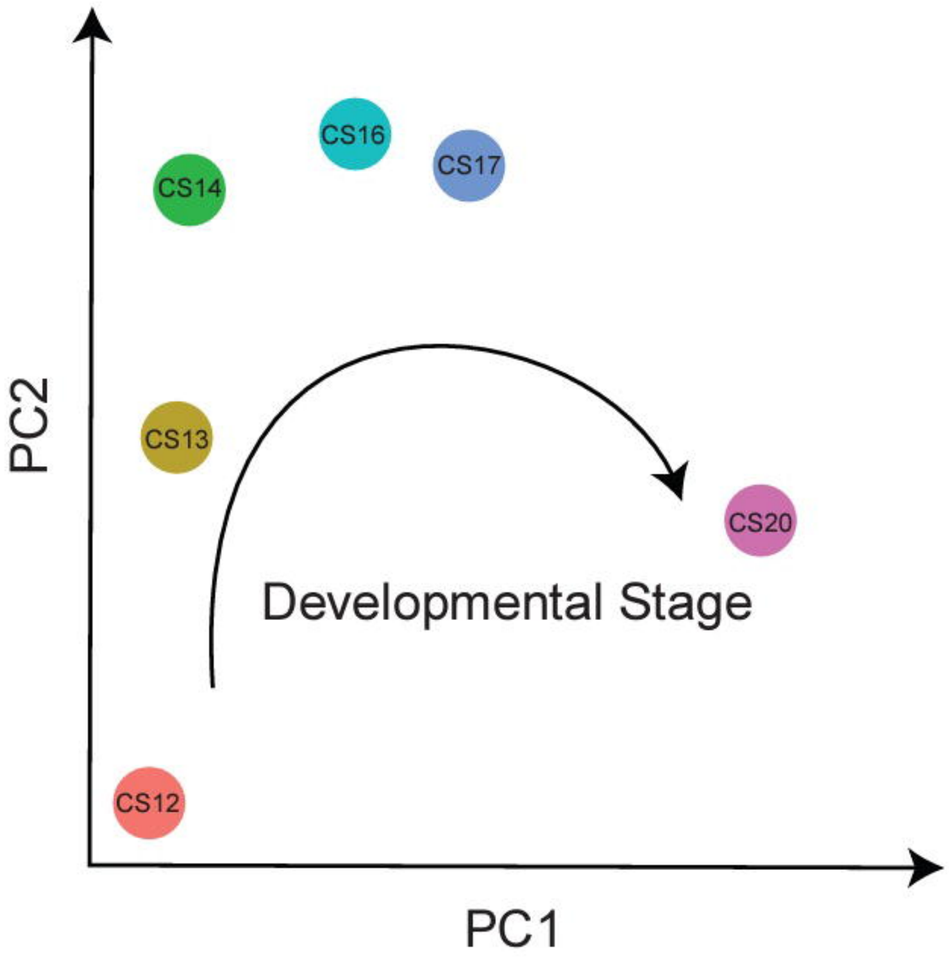

C

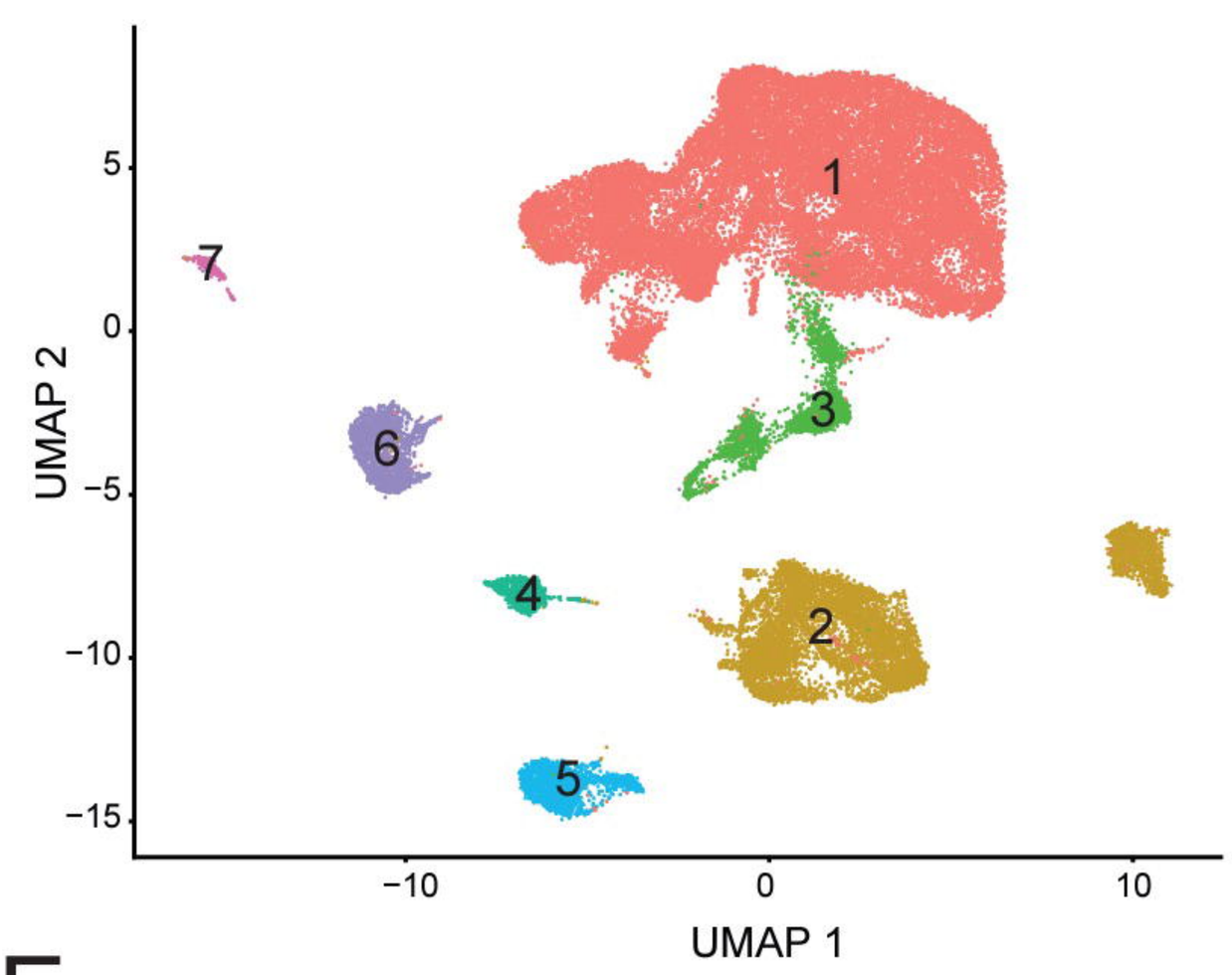

D

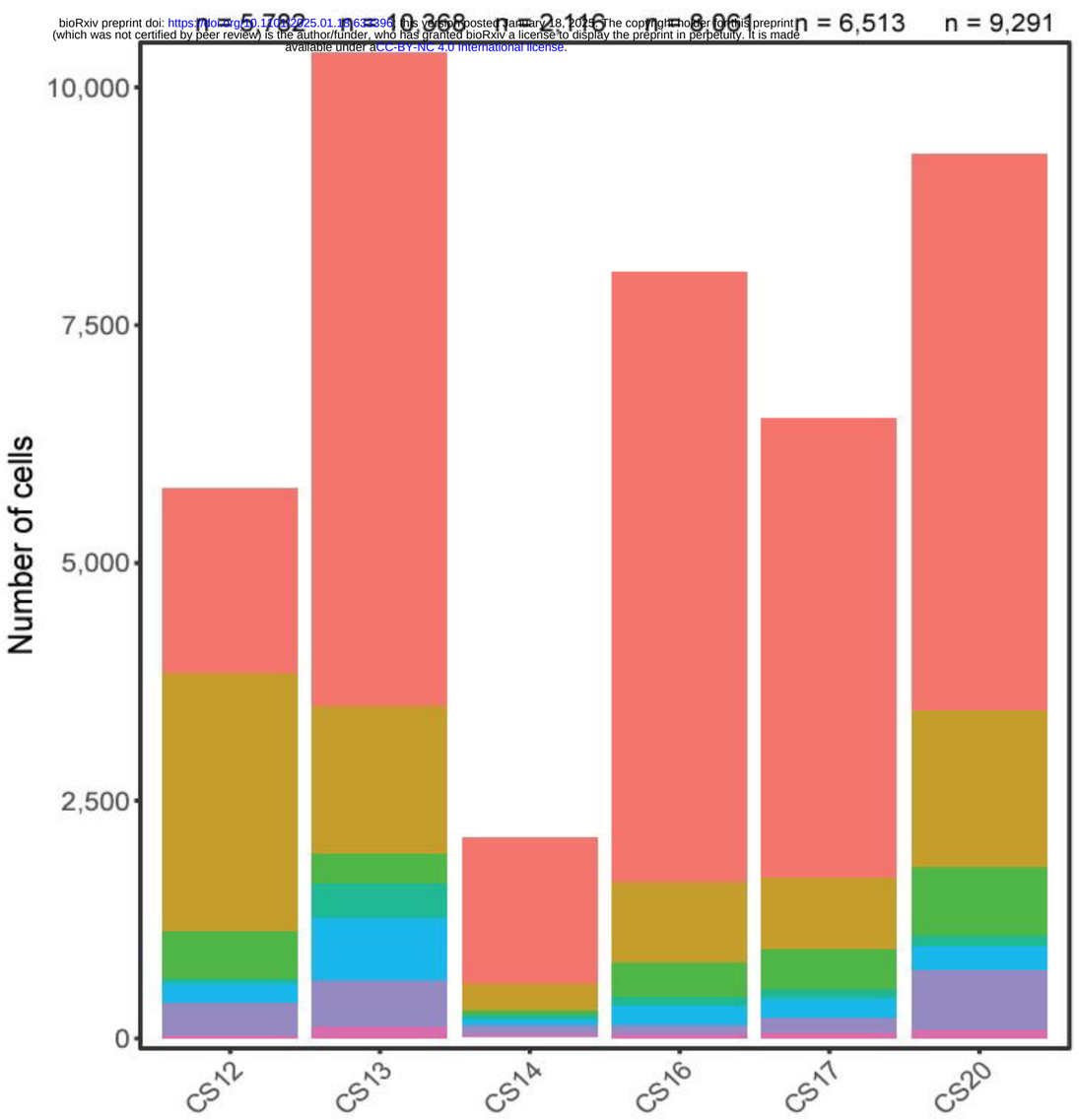

E

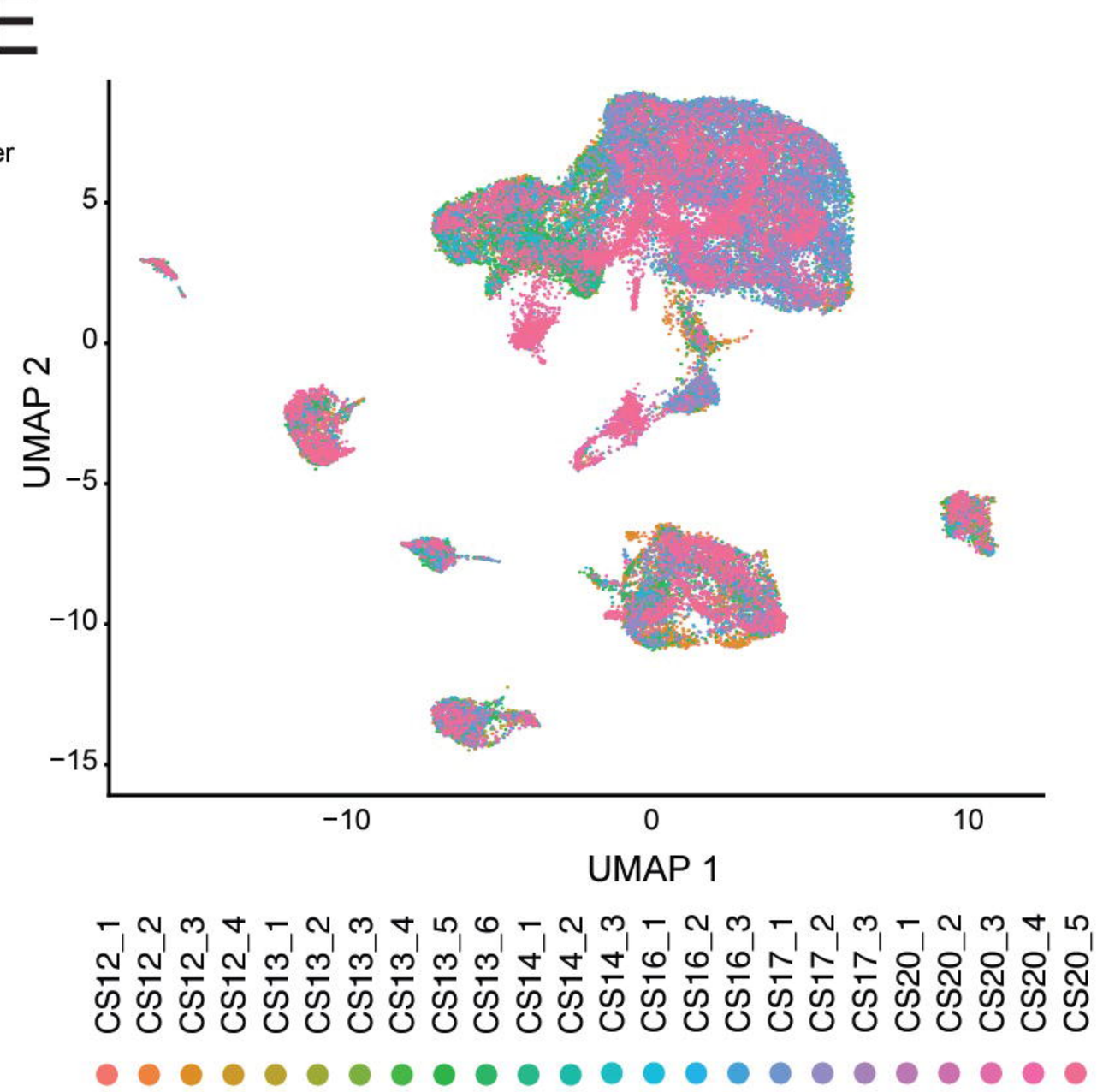

A

ALX1

EPCAM

HEMGN

CDH5

FCER1G

Cluster

B

MNDA
NCF4
MPEG1
MS4A6A
MS4A7
PLEK
CD163
CD86
CYBB
PTPRC
CTXND1
COL20A1
PHOX2B
S100B
ABCA8
SLITRK2
FOXD3
MMP17
INSC
CDH19
ESM1
MYCT1
DIPK2B
CD93
ADGRF5
CDH5
PECAM1
PTPRB
FLT1
KDR
TRIM10
KLF1
CTSE
EPB42
GYPA
RHAG
ALAS2
C17orf99
SPTA1
SLC4A1
MYH3
MYL1
TNNC2
MYOD1
DES
MYOG
CHRNA1
RAPSN
ACTC1
TCF21
OC90
LARGE2
TACSTD2
IRF6
MARVELD3
RASSF6
CLDN3
RGL3
ESRP1
GRHL2
TNFAIP6
PRKG2
FOXF1
VEGFD
RSPO2
HAND2
SATB2
PRRX1
TWIST1
PDGFRA

1 2 3 4 5 6 7

pct.exp
25
50
75

avg.exp
2.0
1.5
1.0
0.5

C

DisGeNet Cluster Enrichments

Craniofacial Abnormalities
Hypoplasia of the maxilla
Congenital Epicanthus
Giant Cell Fibroblastoma
Dermatofibrosarcoma Protuberans
Cleft palate, isolated
Tooth Abnormalities
Uranostaphyloschisis
Aneurysm of ascending aorta
Frontonasal dysplasia
tumor vasculature
Congenital arteriovenous malformation
Childhood Alveolar Rhabdomyosarcoma
Epidermolysis Bullosa
ANONYCHIA
Keratoderma, Palmoplantar
Carcinoma, Papillary
Junctional Epidermolysis Bullosa
Milium Cyst
Dystrophia unguium
Epithelioma
Carcinoma, Large Cell
Sparse body hair
Congenital myopathy (disorder)
Type 1 muscle fiber predominance
Myopathic disorders
Respiratory insufficiency due to
Pena–Shokeir syndrome type I
Myopathies, Nemaline
Familial dilated cardiomyopathy
Neck flexor weakness
Creatine phosphokinase serum increased
Muscular Dystrophy
Acute Erythroblastic Leukemia
Adult Erythroleukemia
Erythroleukemia (Erythroid/Myeloid)
Pallor
Reticulocyte count (procedure)
Anemia, Hemolytic
beta Thalassemia
Reticulocytosis
Hereditary spherocytosis
Hemoglobinopathies
Nephritis
Hemangiosarcoma
Adult Angiosarcoma
Childhood Angiosarcoma
Infantile hemangioma
Acute Coronary Syndrome
Disease of capillaries
High grade glioma
Strawberry nevus of skin
Inflammation
Tumor Immunity
IGA Glomerulonephritis
WAARDENBURG SYNDROME, TYPE 4A
Inherited neuropathies
Peripheral demyelinating neuropathy
Polyneuropathy
Wilson syndrome
CNS disorder
Brain Tumor, Primary
White forelock
Aganglionosis, Colonic
Sarcoidosis
Infection
Tuberculosis, Pulmonary
Diphtheria
Immune System Diseases
Common Variable Immunodeficiency

1 2 3 4 5 6 7

p.adjust
0.01
0.02
0.03

GeneRatio
0.05
0.10
0.15
0.20

D

Cranial Neural Crest Genes Module Score

mesenchyme (1)
ectoderm (2)
muscle (3)
red blood cells (4)
endothelium (5)
CNCC (6)
other
blood cells (7)

−0.5 0.0 0.5 1.0 1.5

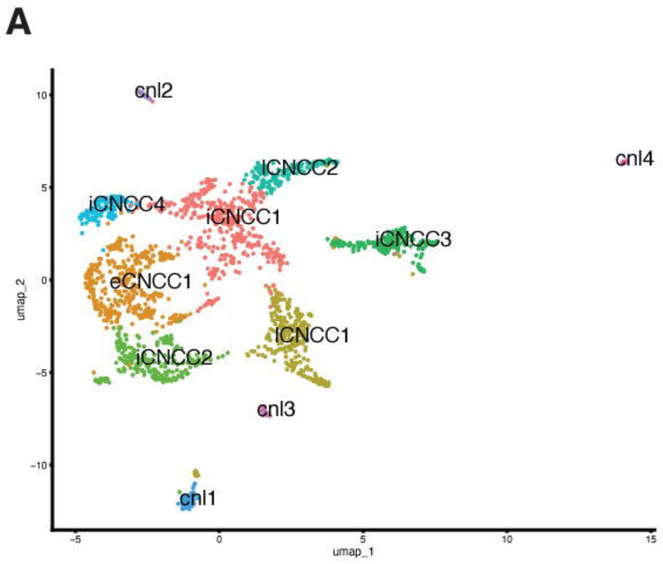

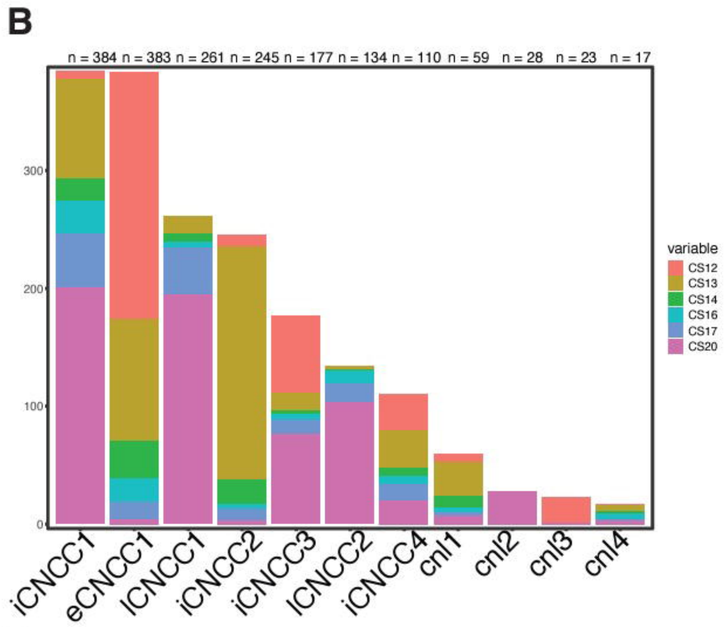

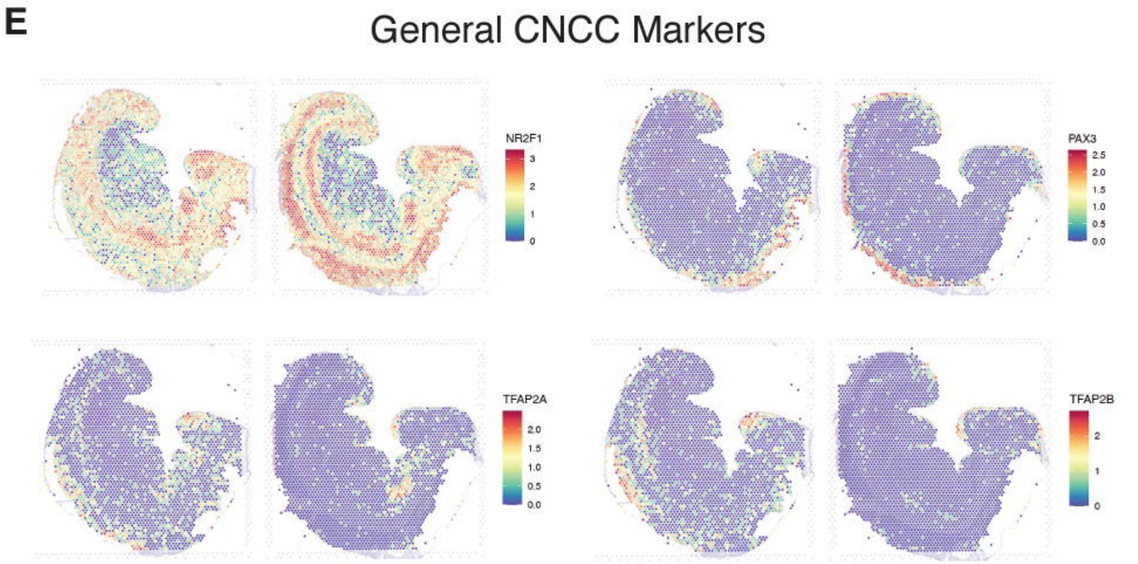

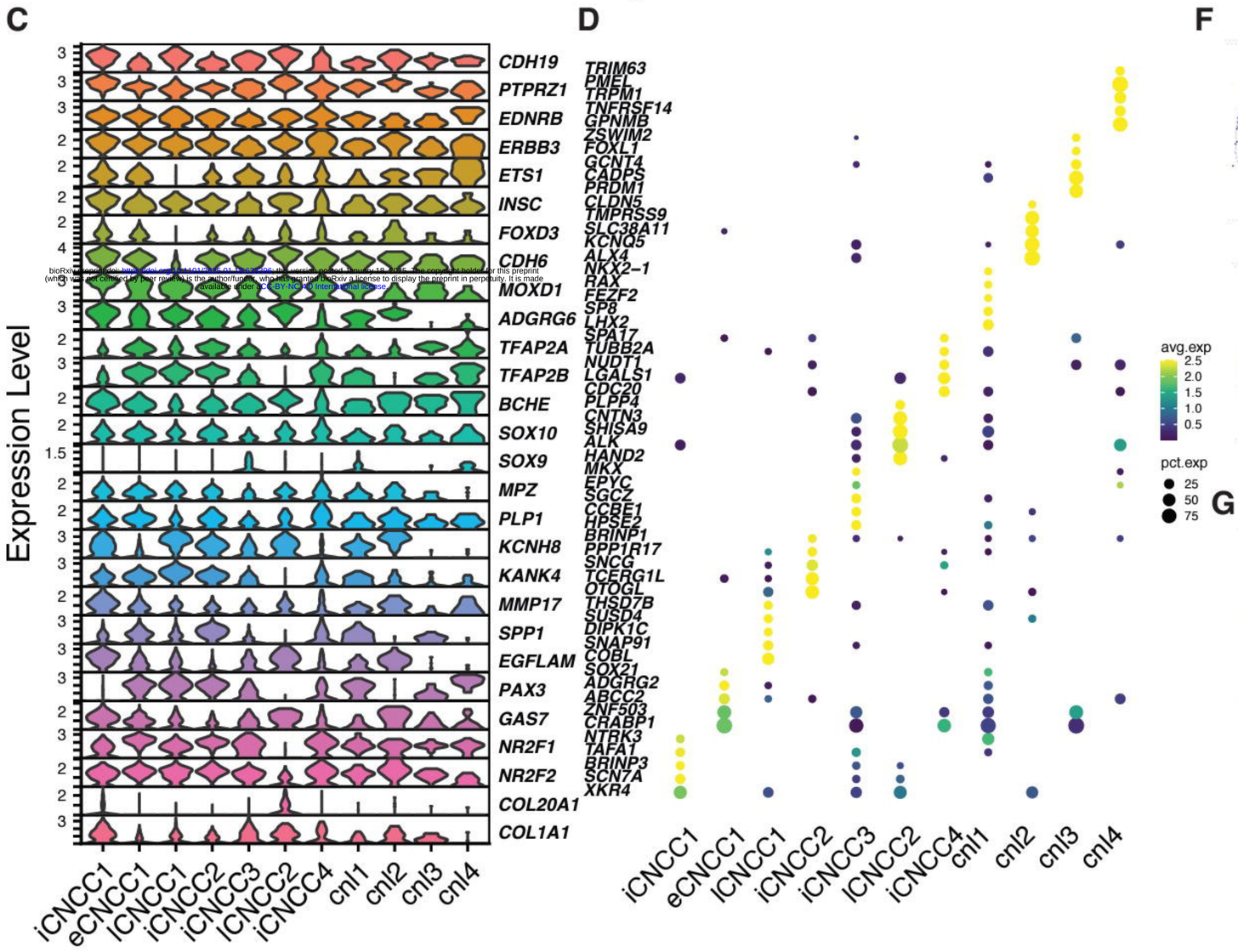

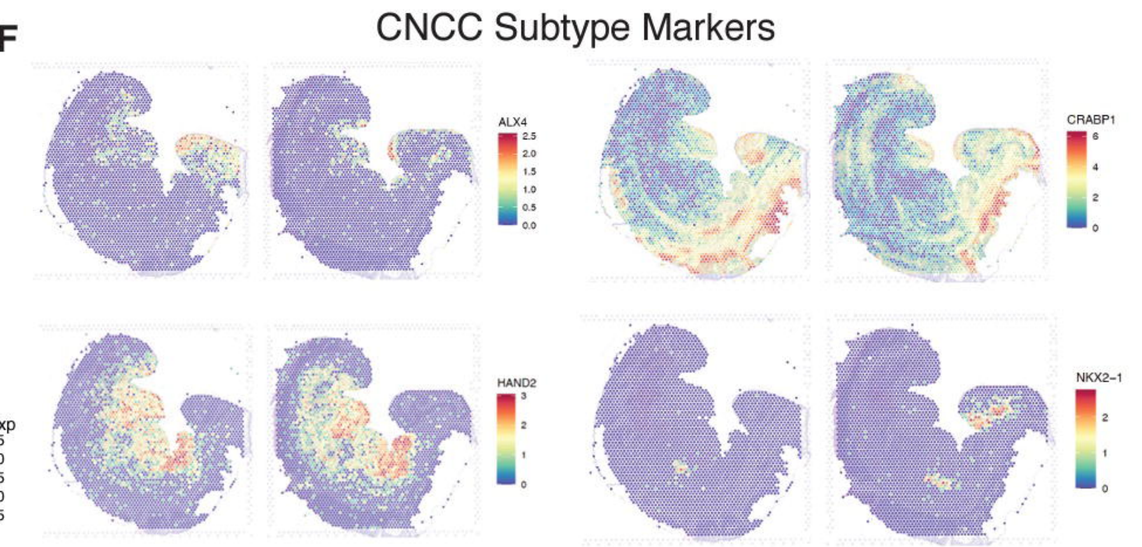

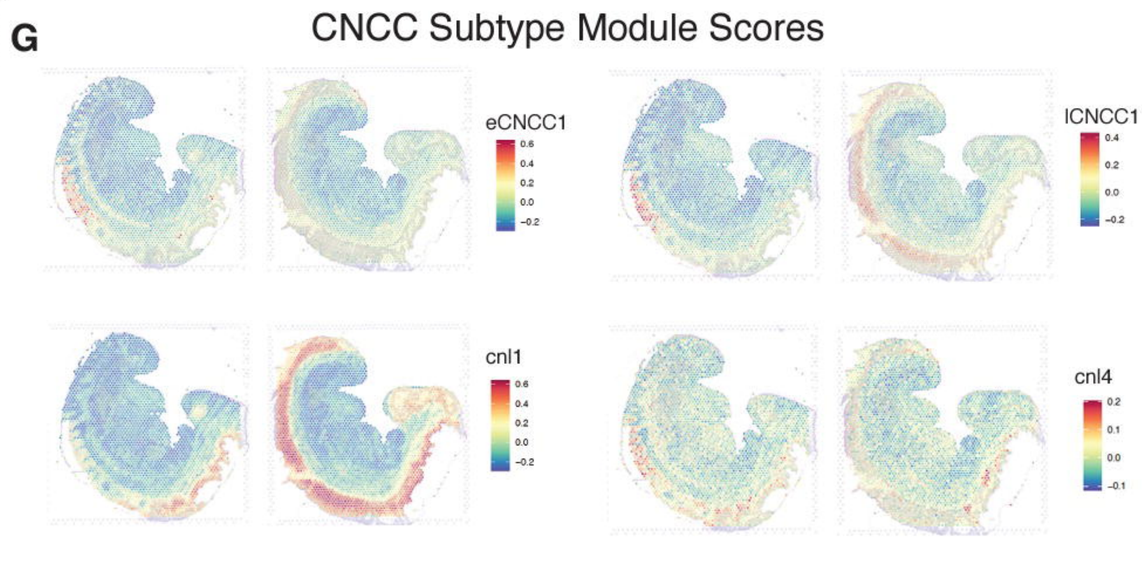

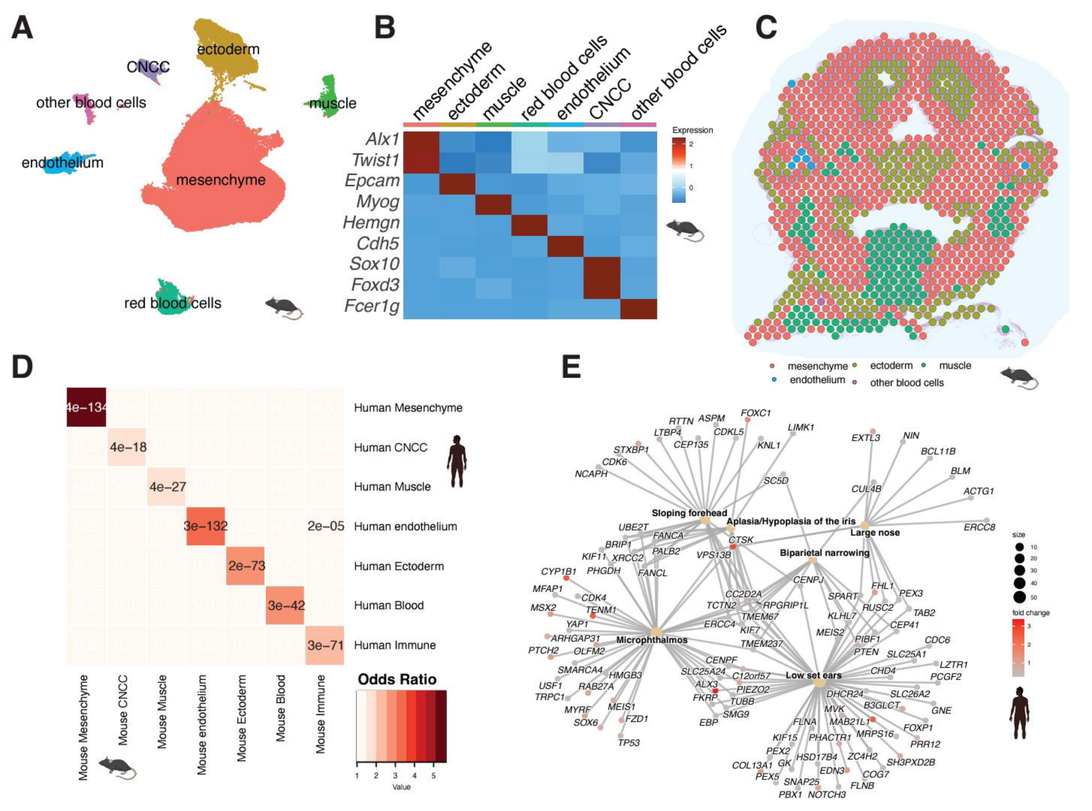

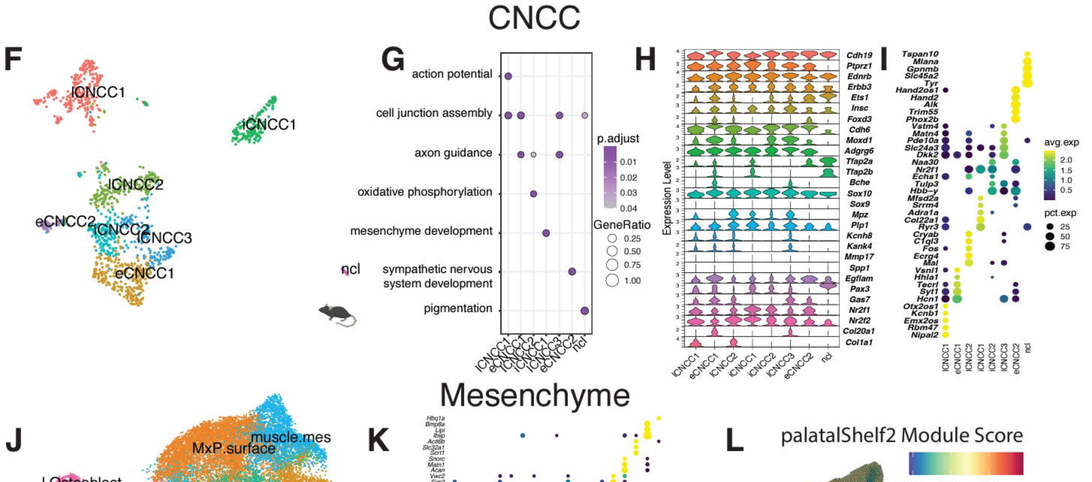

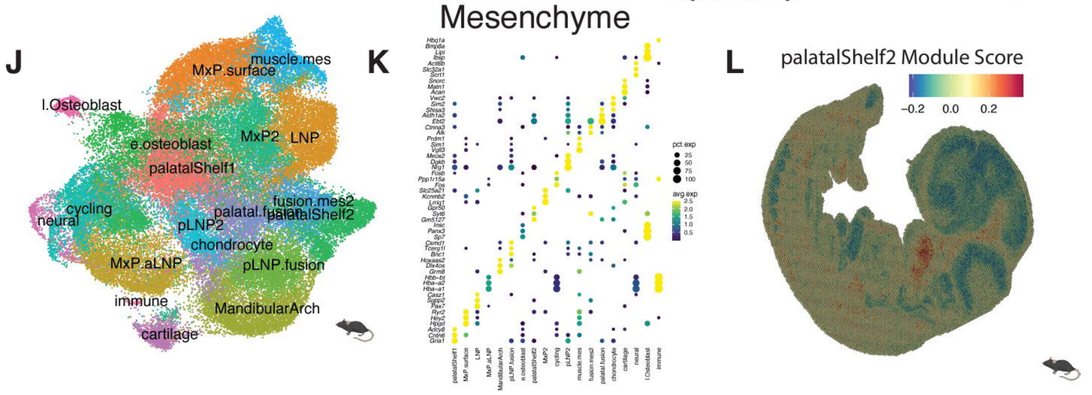

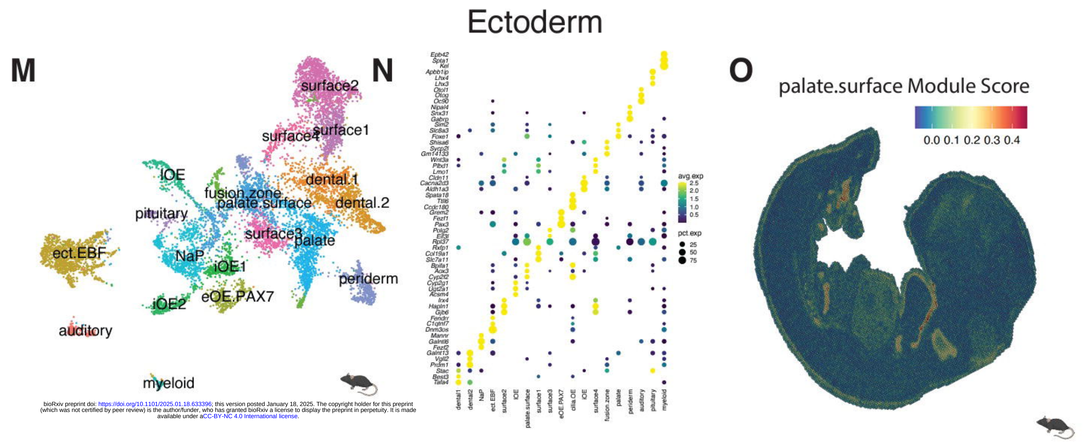

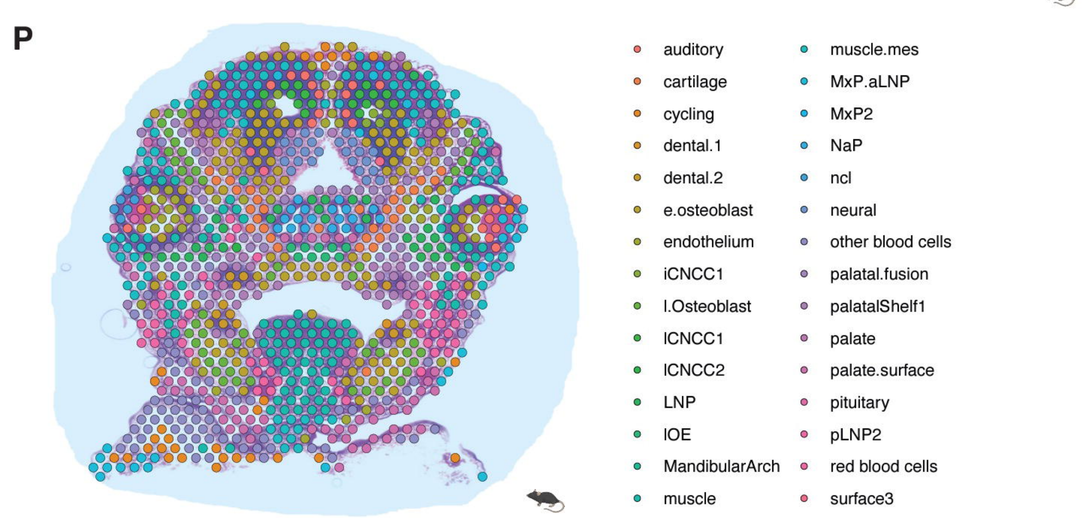

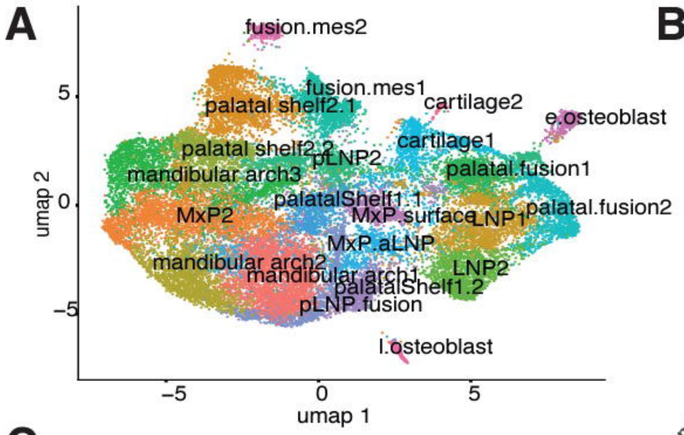

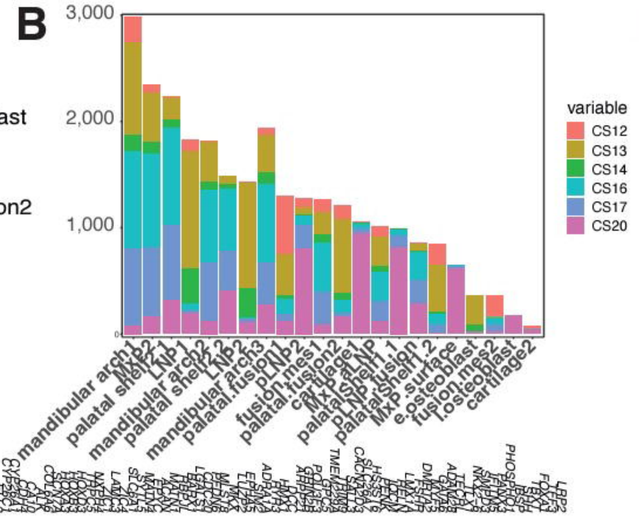

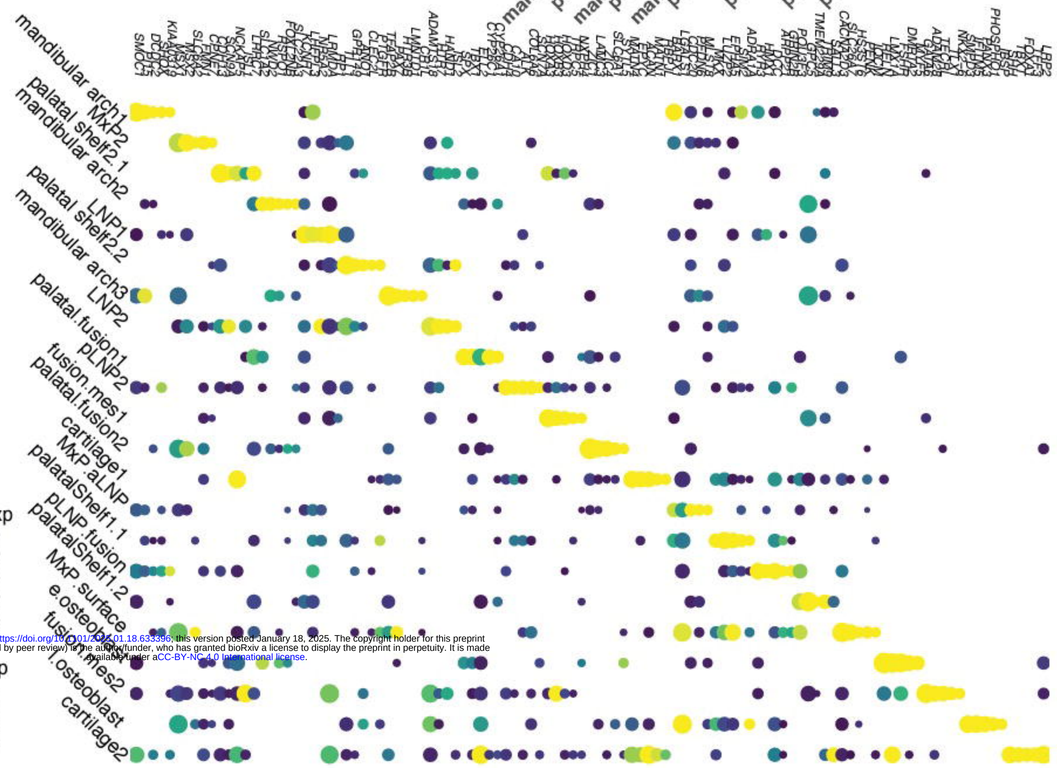

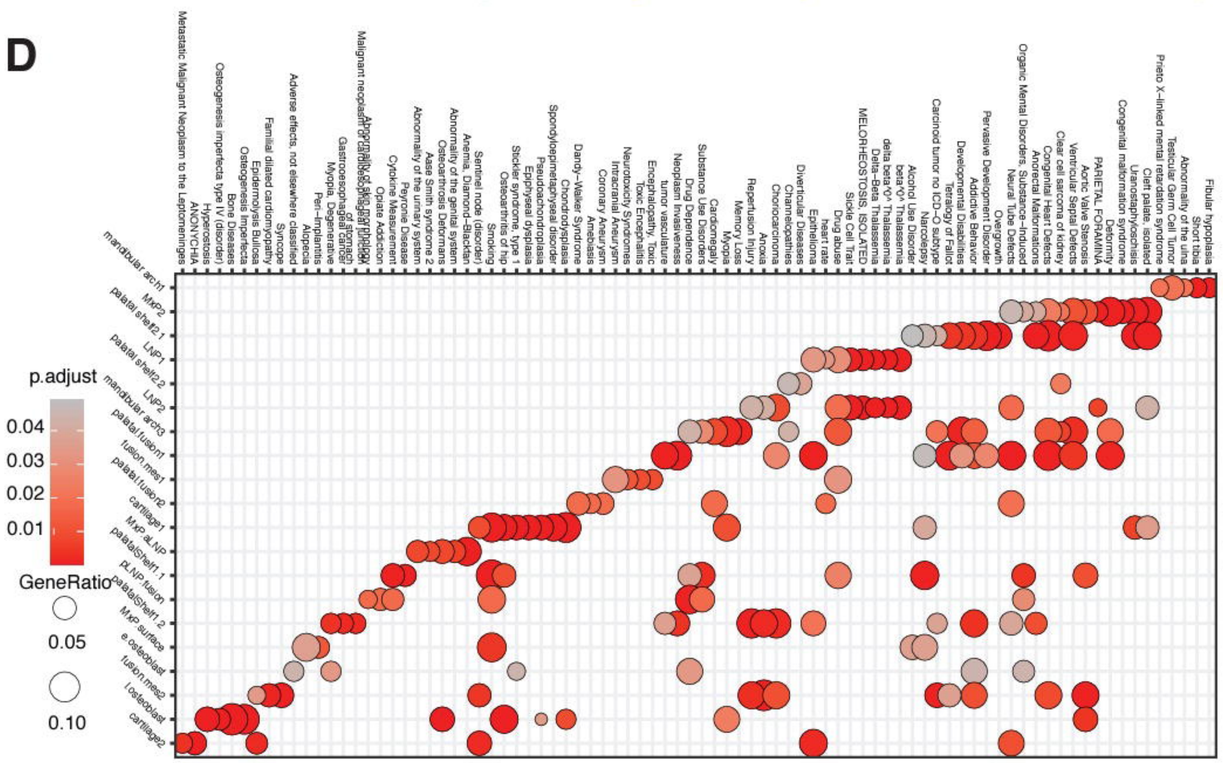

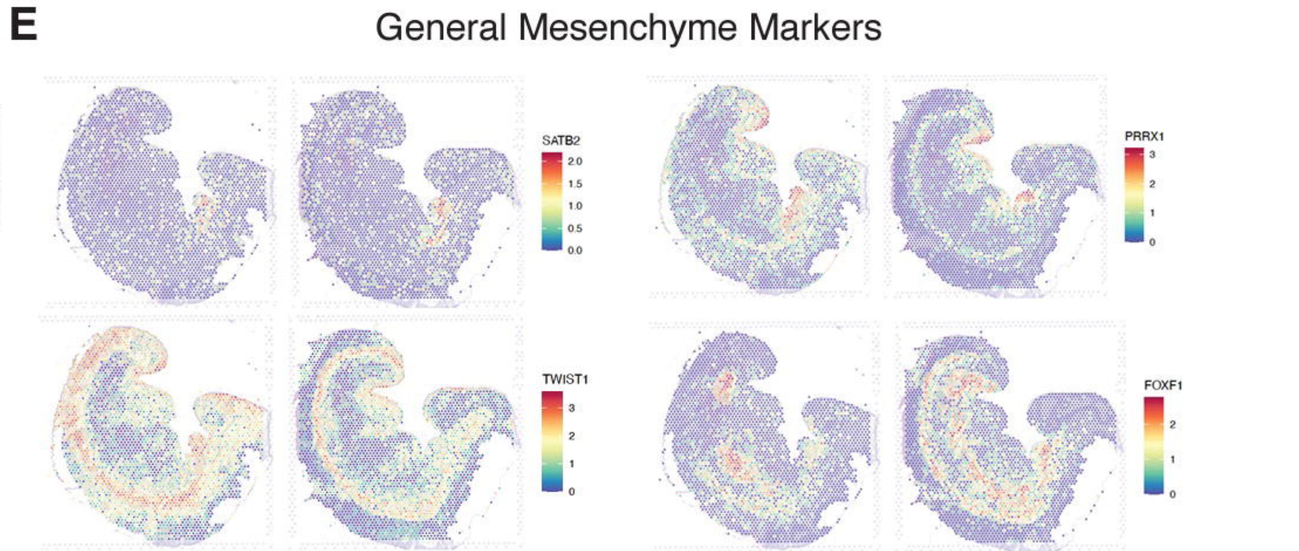

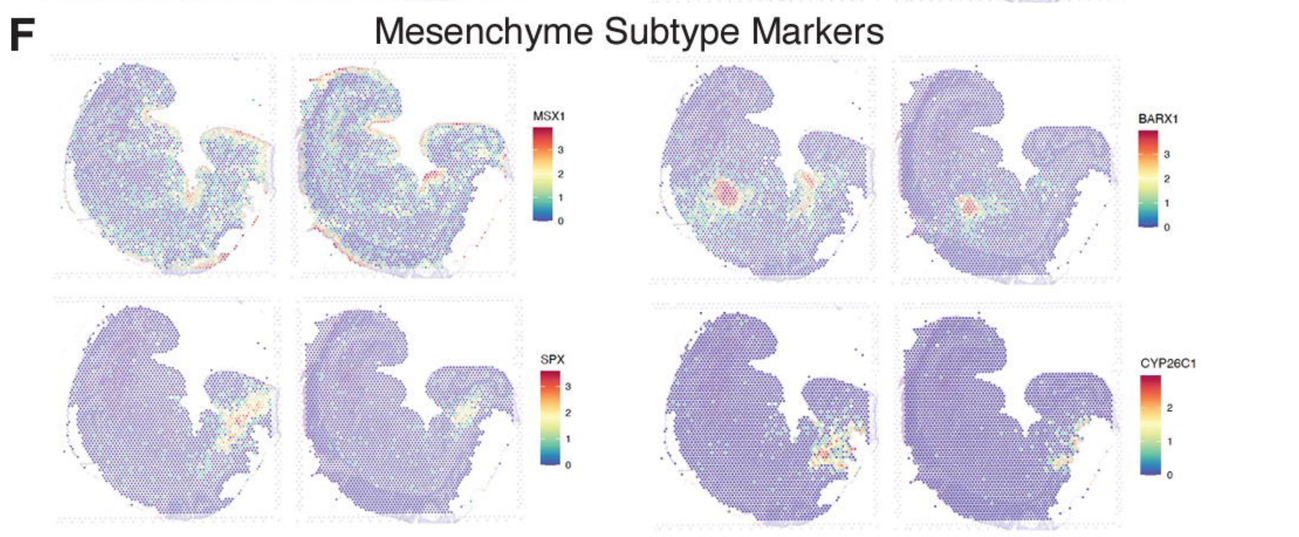

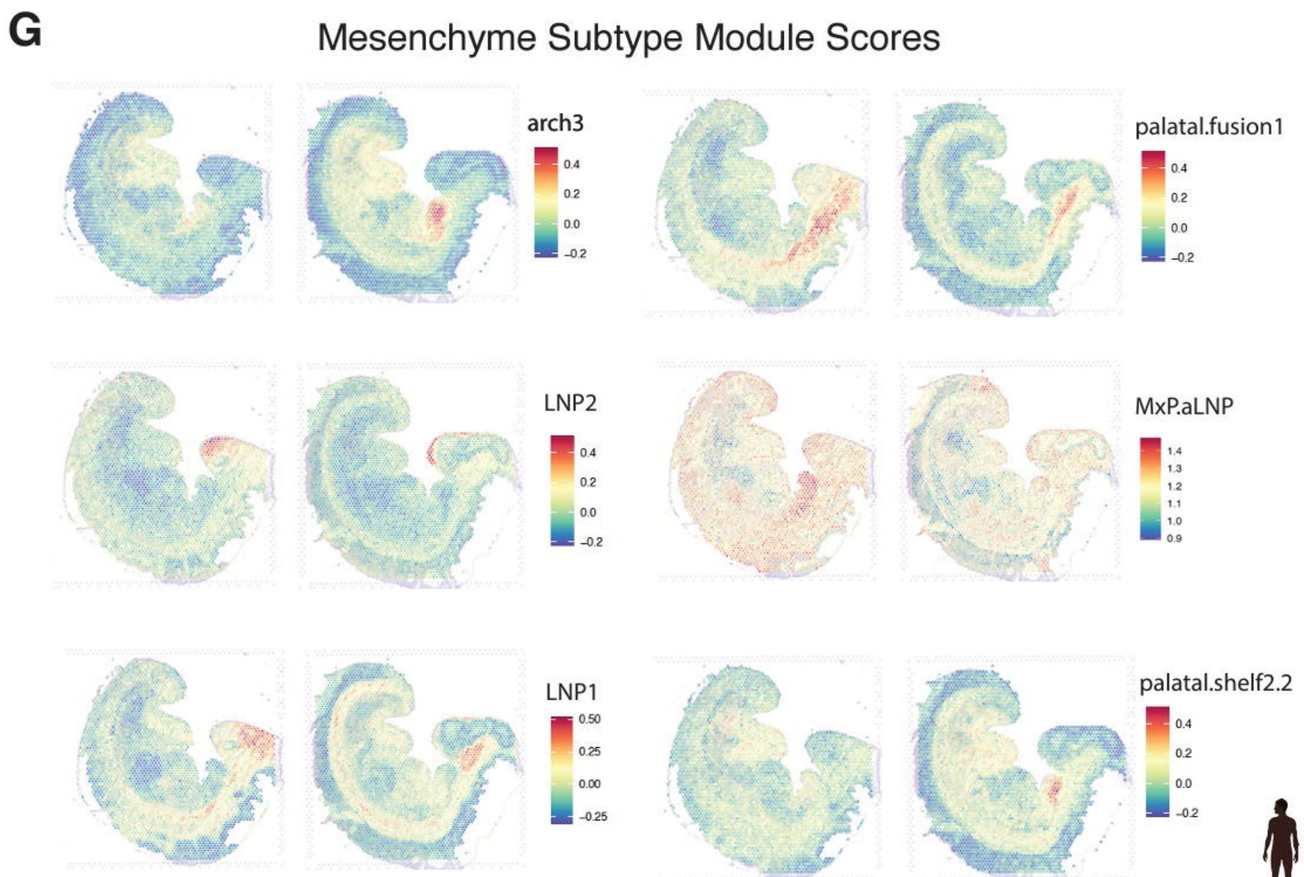

A Craniofacial Variation

main_type
CNCC
Ectoderm
Endothelium
Mesenchyme
Muscle
Other blood cells
Red blood cells

Type
frontal
profile

Region
Ear
Lip
Lower
Mid
Upper

Lower_Lip_Thickness_2
Lower_Lip_Thickness_1
Eye_Position_1
ExR–N
Jaw_Slope_2
Upper_Face_Flatness
Forehead_Protrusion_1
Lip_Thickness_Ratio_1
Lip_Thickness_Ratio_2
Lip_Thickness_1
AlR–ChL
EnR–ChL
Columella_Inclination
Sn–AlR
ExR–ChL
Nose_Protrusion
Brow_Ridge_Protrusion_1
Brow_Ridge_Protrusion_2
Nasion_Depth_2
Nasion_Depth_1
Ear_Size
Nose_Height
Lip_Protrusion
Prn–AlL
N–ExL
EnR–Sn
Nose_Size
Lower_Face_Flatness
Chin_Protrusion_1
Chin_Protrusion_2
N–Prn
Nose_Roundness_1
Nose_Roundness_3
EnR–AlR
Lower_Lip_Protrusion
Columella_Size
Philtrum_Length
ExL–AlL
AlL–AlR
AlL–Sn
EnR–ChR
ExR–ChR
EnR–Prn
Jaw_Protrusion_2
Jaw_Protrusion_5
AlL–Ls
Nasion_Position_2
Brow_Ridge_Protrusion_3
Prn–AlR
EnL–AlL
Prn–Ls
EnR–N
Nostril_Size
EnL–Sn
Prn–EnL

Profile Landmarks
(Bonfante et al 2021)

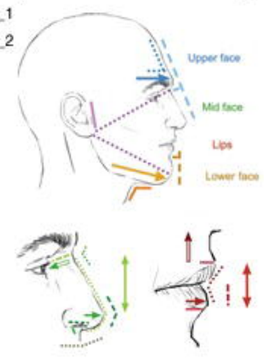

Frontal Landmarks
(Xiong et al 2019)

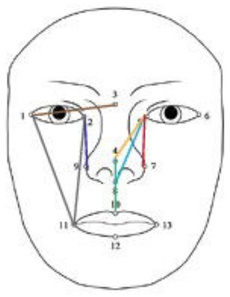

No	Abbreviation	Name
1	ExR	Right Exocanthion
2	EnR	Right Endocanthion
3	N	Nasion
4	Prn	Pronasale
5	EnL	Left Endocanthion
6	ExL	Left Exocanthion
7	AlL	Left Alare
8	Sn	Subnasale
9	AlR	Right Alare
10	Ls	Labiale superius
11	ChR	Right Cheilion
12	Li	Labiale inferius
13	ChL	Left Cheilion

, 0.05 < p < 0.1
★ p < 0.05
★★ p < 0.01
★★★ p < 0.001

B FinnGen Congenital Malformations

main_type
CNCC
Ectoderm
Endothelium
Mesenchyme
Muscle
Other blood cells
Red blood cells

CLEFT_LIP_CLEFT_PALATE
CLEFT_LIP_OR_LIP_AND_PALATE

ANKYLOGLOSSIA
CONGEN_MALFO_TONGUE
MOUTH_PHARYNX

, 0.05 < p < 0.1
★ p < 0.05
★★ p < 0.01
★★★ p < 0.001

C HPO Enrichments

Craniofacial Cell Subtypes
59 cell subtypes

Craniofacial
Main Cell types

Significant associations (normalised)

Abnormal cellular phenotype
(15 phenotypes)
Abnormality of blood / blood–forming tissues
(536 phenotypes)
Abnormality of head or neck
(1047 phenotypes)
Abnormality of limbs
(61 phenotypes)
Abnormality of metabolism/homeostasis
(782 phenotypes)
Abnormality of prenatal development or birth
(92 phenotypes)
Abnormality of the breast
(30 phenotypes)
Abnormality of the cardiovascular system
(672 phenotypes)
Abnormality of the digestive system
(369 phenotypes)
Abnormality of the ear
(210 phenotypes)
Abnormality of the endocrine system
(291 phenotypes)
Abnormality of the eye
(717 phenotypes)
Abnormality of the genitourinary system
(853 phenotypes)
Abnormality of the immune system
(253 phenotypes)
Abnormality of the integument
(671 phenotypes)
Abnormality of the musculoskeletal system
(2147 phenotypes)
Abnormality of the nervous system
(1644 phenotypes)
Abnormality of the respiratory system
(292 phenotypes)
Abnormality of the thoracic cavity
(2 phenotypes)
Abnormality of the voice
(15 phenotypes)
Constitutional symptom
(61 phenotypes)
Growth abnormality
(83 phenotypes)
Neoplasm
(77 phenotypes)

auditory1
auditory2
auditory3
cartilage1
cartilage2
cnl1
cnl2
cnl3
cnl4
dental
e.dental
e.osteoblast
eCNCC1
ect.EBF
ect.GDNF
endothelium
eOE
eye.ect
fusion.mes1
fusion.mes2
fusion.zone
iCNCC1
iCNCC2
iCNCC3
iCNCC4
iOE1
iOE2
l.osteoblast
lCNCC1
lCNCC2
LNP1
LNP2
mandibular arch1
mandibular arch2
mandibular arch3
muscle
MxP.aLNP
MxP.surface
MxP2
myeloid
NaP
OE3
other blood cells
palatal shelf2.1
palatal shelf2.2
palatal.fusion1
palatal.fusion2
palatalShelf1.1
palatalShelf1.2
palate
palate.surface
periderm
pituitary
pLNP.fusion
pLNP2
red blood cells
surface2
surface3
thyroid

CNCC
ectoderm
endothelium
mesenchyme
muscle
other blood cells
red blood cells

★ p < 0.05
★★ p < 0.01
★★★ p < 0.001